Journal of Energy Storage 64 (2023) 107150

Contents lists available at ScienceDirect

Journal of Energy Storage

journal homepage: www.elsevier.com/locate/est

Research papers

A physics-based fractional-order equivalent circuit model for time and frequency-domain applications in lithium-ion batteries

Pablo Rodríguez-Iturriaga [a,*], David Anseán [b], Salvador Rodríguez-Bolívar [a], Manuela González [b], Juan Carlos Viera [b], Juan Antonio López-Villanueva [a]

[a] Department of Electronics and Computer Technology, Faculty of Sciences, University of Granada, Granada, 18071, Andalusia, Spain
[b] Department of Electrical Engineering, Polytechnic School of Engineering, University of Oviedo, Gijon, 33204, Asturias, Spain

ARTICLE INFO

Keywords:
Lithium-ion battery
Equivalent circuit model
Fractional-order model
Physics-based model
EIS

ABSTRACT

Equivalent circuit models (ECMs) remain the most popular choice for online applications in lithium-ion batteries because of their simpler parameterization and lower computational requirements in comparison to electrochemical models. Nevertheless, standard ECMs lack physical insight and fail to accurately reproduce cell behavior under a wide range of operating conditions. For this reason, the development of physics-informed ECMs becomes essential so as to provide a better description of the physical processes while maintaining a reduced computational complexity. In this article, we propose a novel physics-based ECM derived directly from an electrochemical model, so that there is a clear correlation between circuit states and internal battery states, as well as circuit and physical parameters. The proposed model yields an RMS error below 1.46 mV for cell voltage, 0.28% for the surface concentration in the active material particles, 0.6% for the electrode-averaged electrolyte concentration and 0.32 mV for the charge-transfer overpotentials. Another key feature of this model is the relationship between circuit parameters and those identified in frequency-domain tests, which allows us to characterize and validate the model experimentally. We understand that the presented model constitutes an alternative to standard ECMs as well as electrochemical models as it combines advantageous characteristics from both of them.

1. Introduction

As concerns over energy supply and environmental issues grow larger worldwide, electrochemical energy storage has become a subject of intense research. In particular, rechargeable lithium-ion batteries have materialized as the leading storage solution for a number of applications [1–3], due to their high energy density, high specific energy, and low self-discharge [4]. Therefore, the development of comprehensive battery models is critical for their online monitoring by a Battery Management System (BMS) [5], thus ensuring their safe operation as well as a prolonged useful lifespan by accurately estimating internal battery states [6]. Three broad groups are commonly considered in the field of battery modeling: physics-based models, equivalent circuit models (ECMs) and data-driven models [4,7]. In data-driven approaches the battery is substituted by a black-box model that is able to reproduce its behavior. Nevertheless, the validity of the resulting model relies heavily on the training dataset. This may lead to practical drawbacks, such as a considerably time-consuming training process or overfitting issues [7]. Consequently, electrochemical and equivalent circuit models continue to be of great research interest, and we will focus on them in this study.

Physics-based approaches model the physical processes and electrochemical reactions that occur in the cell, with the Doyle–Fuller–Newman (DFN) [8,9] being considered the standard battery model. Due to its complex nature, several approximations have been proposed so as to maintain the description of the physical processes with a restrained computational load [10], with the Single Particle Model (SPM) [11,12] being one of the most widely used. The SPM makes the assumptions that each electrode is composed of spherical active material particles with the same physical properties and that electrolyte dynamics are negligible [13], so the current distribution is uniform across the electrode. Consequently, only one representative particle from each electrode needs to be taken into account. This approximation holds true for low current rates [14]; however, at moderate and large currents the effects of concentration and potential gradients in the electrolyte should be accounted for. Therefore, several approaches have been proposed to include electrolyte dynamics with the goal of extending the range of applicability of the SPM [14–18],

* Corresponding author.
E-mail address: priturriaga@ugr.es (P. Rodríguez-Iturriaga).

https://doi.org/10.1016/j.est.2023.107150
Received 22 December 2022; Received in revised form 16 February 2023; Accepted 14 March 2023
Available online 22 March 2023

usually by the names 'enhanced SPM' (eSPM) or 'SPM with electrolyte (SPMe)', via polynomial approximations of the electrolyte concentration profile [15,16,18] or the numerical resolution of the corresponding PDE [14,17,18], with the former approach being less suitable for pulsed currents [19]. There also exist some alternatives to the direct numerical resolution of the PDEs, in which the transfer functions of the system are obtained from electrochemical models and then transformed into a discrete state-space representation with the Discrete-Time Realization Algorithm (DTRA) [20] or into a SIMULINK [21] model via simplified fractional-order transfer functions [22–24]. Nevertheless, these models still require a precise set of physical parameters, whose determination from non-invasive experimental measurements continues to be an open research topic [25].

On the other hand, ECMs approximate the electrical behavior of a battery cell by that of a specific circuit. This approach is characterized by reduced memory requirements and a low computational load, therefore making them appropriate for online BMSs [26–29]. Moreover, their discrete state-space representation is easily obtained, thus allowing for the implementation of state observers and Kalman filters [30–32] to mitigate the influence of measurement and process noise. The challenge is twofold when developing ECMs: first, determining which circuit topology reproduces battery behavior more accurately, and secondly, obtaining the corresponding parameter values for said topology from experimental tests [33–35]. Most ECMs include a voltage source, which corresponds to the open-circuit voltage (OCV) as a nonlinear function of the cell state of charge (SOC), in series with the internal ohmic resistance and one or several parallel RC elements that model dynamic behavior [30]. A variation, useful for circuit simulators, substitutes the independent OCV source by a voltage source dependent on the state of charge of a capacitor which represents battery SOC [36]. However, these models introduce a strong separation between quasi-static electrode thermodynamics included in the OCV-SOC relationship [37] and the dynamic behavior represented by the RC network, in which different diffusion processes are mixed and a direct equivalence with the internal states of the battery is not often possible. Additionally, physics-based models show that electrode potential is dependent on the lithium concentration at the surface of active material particles rather than their average concentration, which is what SOC stands for. The difference between both magnitudes may be considerably large at high current rates, as predicted by the SPM [38]. Li et al. [39] recently proposed a modification to the model by Chen and Rincon-Mora [36] by which the non-linear voltage source depends on an intermediate variable named SOC_{surf}, which is obtained as the result of the series connection of the SOC capacitor and a RC-element that represents the non-uniform concentration profile due to lithium diffusion in the active material particles. Nevertheless, the relationship between circuit parameters and their physical counterparts is generally lost, which makes these models inaccurate outside the range in which they have been determined experimentally.

For these reasons, several works combine an equivalent circuit model for electrolyte dynamics and ohmic losses with the transfer functions for solid diffusion in physics-informed reduced order models [40–43]. These works make use of Padé's method in order to obtain rational approximations to these transcendental transfer functions. However, it has to be pointed out that Padé's approximants are calculated in the neighborhood of a certain point, typically the frequency $s = 0$, so the accuracy of the approximation is not guaranteed within the whole frequency range. Furthermore, it has been shown that diffusion processes are more accurately modeled by a continuous distribution of time constants [44], therefore suggesting that fractional-order transfer functions are more appropriate in this context. This is also corroborated by Electrochemical Impedance Spectroscopy (EIS) tests [6,44–47]. The Nyquist plot of EIS data shows several depressed semicircles and constant-slope tails that may be modeled electrically by Constant-Phase Elements (CPEs) [48] and ZARC elements [49], which are the parallel connection of a resistor and a CPE. The introduction of fractional-order circuit elements entails the computation of fractional-order derivatives, so several approaches have been proposed in the literature for approximating their behavior in the time domain [49–53]. Moreover, fractional-order ECMs have been employed successfully in conjunction with Kalman filters in recent years [54–56] for the concurrent estimation of battery state of charge and electrical parameters.

For all the reasons above, the development of a physics-based ECM, which is able to provide information about internal battery states and whose circuit parameters are directly correlated with physical parameters, is an open research topic. Furthermore, we also consider the relationship between the time-domain and frequency-domain behaviors of lithium-ion batteries to be a subject of interest. Therefore, in this article we derive a novel reduced fractional-order ECM from an electrochemical model, whose states and parameters are related to those of the battery cell. Additionally, we have analyzed the correspondence between said circuit parameters and those identified from EIS measurements, thus clarifying the connection between frequency-domain data and physical parameters. For this purpose, we have obtained simplified transfer functions from the SPMe and determined their electrical equivalent with fractional-order elements. Subsequently, the proposed model has been validated first against the SPMe for given a parameter set, and next with experimental data by identifying equivalent circuit parameters from EIS measurements. The major advantage of this model over previous ECMs is the extended insight into the internal battery states and physical processes, whereas it groups physical parameters in resistors and time constants and presents lower computational requirements with respect to the SPMe, thus allowing for a simpler parameterization process as well as the implementation of online estimation algorithms.

The main contributions of this article are condensed as follows:

1. Deriving reduced transfer functions directly from the SPMe and establishing their electrical equivalent via ZARC elements, as well as the criteria for the validity of the employed approximations.
2. Constructing an equivalent circuit model whose parameter values are directly correlated with their physical counterparts, and whose states contain information about the internal states of the battery cell.
3. Providing a method to determine said equivalent circuit parameters from EIS data, thus bridging the gap between the time and frequency-domain behaviors of lithium-ion batteries.

In consequence, this paper is structured as follows: the analytical derivation of the proposed equivalent circuit model is presented in Section 2. The theoretical validation against an electrochemical model is carried out in Section 3, whereas the experimental parameterization process and results are detailed and discussed in Section 4. Some final remarks are provided in the last section.

2. Equivalent circuit development

In this section, the procedure to obtain simplified transfer functions from the SPMe and their electrical equivalence is described with the goal of developing an equivalent circuit model. The main advantage of employing the SPMe instead of the DFN as in [20] lies in the fact that the former removes the coupling between the partial differential equations. Therefore, each diffusion process may be analyzed independently, thus producing considerably simpler transfer functions and allowing for a direct electrical equivalence.

2.1. SPMe model description

Marquis et al. [14] proposed an SPMe derived as an asymptotic reduction of the standard DFN model, which expresses battery terminal voltage as a function of electrode-averaged quantities. In said model, the output voltage is split into the sum of its components as in Eq. (1):

$$V = U_{eq} + \eta_c + \eta_r + \Delta\Phi_e + \Delta\Phi_s \tag{1}$$

where the term U_{eq} stands for the equilibrium potential, η_c and η_r represent the voltage drop due to concentration gradients in the electrolyte and charge-transfer reactions, respectively, and $\Delta\Phi_e$ and $\Delta\Phi_s$ are the ohmic losses in the electrolyte and solid, respectively. The detailed expression for each term is shown in Eq. (2):

$$U_{eq} = OCP_p(\chi_p|_{r=R_p}) - OCP_n(\chi_n|_{r=R_n}) \tag{2a}$$

$$\eta_c = \frac{2RT}{F}\frac{(1-t^+)}{c_{e,typ}}\left(\bar{c}_{e,p} - \bar{c}_{e,n}\right) \tag{2b}$$

$$\eta_r = \frac{2RT}{F}\left[\sinh^{-1}\left(\frac{IR_p}{6j_{0,p}\epsilon_p L_p A}\right) + \sinh^{-1}\left(\frac{IR_n}{6j_{0,n}\epsilon_n L_n A}\right)\right] \tag{2c}$$

$$\Delta\Phi_e = \frac{I}{\kappa A}\left(\frac{L_n}{3\epsilon_{e,n}^b} + \frac{L_s}{\epsilon_{e,s}^b} + \frac{L_p}{3\epsilon_{e,p}^b}\right) \tag{2d}$$

$$\Delta\Phi_s = \frac{I}{3A}\left(\frac{L_n}{\sigma_n} + \frac{L_p}{\sigma_p}\right) \tag{2e}$$

where OCP_p and OCP_n are the open-circuit potentials for the positive and negative electrodes, respectively. $\chi_p|_{r=R_p}$ and $\chi_n|_{r=R_n}$ are the normalized lithium concentrations in the positive and negative active material particles, respectively, evaluated at their surface, with R_p and R_n being their respective particle radius. Regarding the electrolyte, t^+ is the cation transference number, κ represents the electrode conductivity and $\bar{c}_{e,p}$ and $\bar{c}_{e,n}$ are the electrode-averaged electrolyte concentrations in the positive and negative electrode, respectively. $j_{0,p}$, $j_{0,n}$, σ_p, σ_n ϵ_p and ϵ_n are the exchange current densities, conductivities and active material volume fractions for both electrodes. L_n, L_s, L_p, $\epsilon_{e,p}$, $\epsilon_{e,s}$ and $\epsilon_{e,n}$ represent the thickness and porosities of the positive electrode, separator and negative electrode, respectively. Lastly, A stands for the electrode area, b is the Bruggeman coefficient and I is the current applied to the cell. Note that we have changed the current sign criterion to positive while charging in order to obtain impedance expressions with a positive real part.

The terms that depend directly on solid or electrolyte concentrations (i.e., U_{eq} and η_c) are those that will exhibit a time-domain transient or a frequency response, therefore they will be analyzed in Sections 2.2 and 2.3. The term η_r depends on said concentrations indirectly, so it will be studied subsequently in Section 2.4. The equivalent circuit model along with its discrete state-space representation is presented in Section 2.5 and its correspondence with frequency-domain data is analyzed in Section 2.6.

2.2. Solid diffusion transfer function

To obtain the frequency response of the U_{eq} term in Eq. (2), the evaluation of the lithium concentration at the surface of the solid particles of the electrodes is necessary. If the particles are assumed to be spherical, the diffusion process taking place within them is described by Eq. (3) [14]:

$$\frac{\partial c_s(r,t)}{\partial t} = \frac{D_s}{r^2}\frac{\partial}{\partial r}\left(r^2\frac{\partial c_s(r,t)}{\partial r}\right) \tag{3}$$

with the following boundary conditions [14]:

$$\left.\frac{\partial c_s(r,t)}{\partial r}\right|_{r=0} = 0, \qquad \left.\frac{\partial c_s(r,t)}{\partial r}\right|_{r=R_s} = \frac{IR_s}{3AFL_eD_s\epsilon_s} \tag{4}$$

where r is the distance along the particle radius, c_s is the lithium concentration in the solid, D_s is the lithium diffusion coefficient in the solid, R_s is the particle radius, A is the electrode area, F is Faraday's constant and L_e is the electrode length. The variation in concentration with respect to the initial value is taken as the equation variable, so as to have zero initial time conditions:

$$\tilde{c}_s = c_s - c_{s,0} \tag{5}$$

Upon solving, applying the boundary conditions in Eq. (4) and evaluating at $r = R_s$, the transfer function from the applied current to the variation in surface concentration is obtained in Eq. (6):

$$\frac{\tilde{c}_{s,s}(s)}{I(s)} = \frac{\tau_s}{3\epsilon_s AFL_e}\frac{1}{\sqrt{\tau_s s}\coth\left(\sqrt{\tau_s s}\right) - 1} \tag{6}$$

where τ_s is defined as $\frac{R_s^2}{D_s}$. If normalized concentration is considered instead, the transfer function may be rewritten as in Eq. (7):

$$G_s(s) = \frac{\tilde{\chi}_{s,s}(s)}{I(s)} = \frac{K_s}{\sqrt{\tau_s s}\coth\left(\sqrt{\tau_s s}\right) - 1} \tag{7}$$

where $\tilde{\chi}_{s,s} = \tilde{c}_{s,s}(s)/c_{s,max}$ and $K_s = \frac{\tau_s}{3\epsilon_s AFL_e c_{s,max}}$.

Taking into account that for small values of x, $\sqrt{x}\coth\left(\sqrt{x}\right) \approx 1 + \frac{x}{3} - \frac{x^2}{45}$, one can study the behavior of $G_s(s)$ in the limits $s \to 0$ and $s \to \infty$ as in Eq. (8):

$$G_s(s) \approx \begin{cases} \frac{3K_s}{\tau_s s} + \frac{K_s}{5}, & s \to 0 \\ 0, & s \to \infty \end{cases} \tag{8}$$

In order to approximate the frequency response of $G_s(s)$ between these two limits, in this article we propose a transfer function composed of the addition of an integrator and a ZARC element as expressed in Eq. (9):

$$\frac{K_s}{\sqrt{\tau_s s}\coth\left(\sqrt{\tau_s s}\right) - 1} \approx \frac{3K_s}{\tau_s s} + \frac{K_s/5}{1 + \left(\beta_s\tau_s s\right)^{\alpha_s}} \tag{9}$$

Therefore, α_s and β_S need to be determined so as to obtain the closest approximation to $G_s(s)$. For this purpose, the frequency response of both transfer functions is plotted in a Nyquist diagram and the weighted impedance error between the exact and the approximate transfer function is minimized within a range of frequencies. In this case, we have considered the interval $\omega = \left[\frac{1}{\tau_s}, \frac{10^3}{\tau_s}\right]$ due to the fact that at frequencies lower than $\frac{2\pi}{\tau_s}$ the integrator behavior is dominant, whereas at frequencies higher than $\frac{2\pi\cdot 10^3}{\tau_s}$ the amplitude of the frequency response approaches 0. The resulting values are $\alpha_s = 0.82$ and $\beta_s = 0.0207$, and the Nyquist plot of the frequency response of both transfer functions is shown in Fig. 1.

Note that Eq. (9) is expressed in terms of the normalized frequency $\tau_s s$, so this approximation remains valid regardless of the specific physical parameter values. Furthermore, the fact that the identified order exponent is not equal to 1 proves that a parallel-RC element would not be the most appropriate alternative for approximating the original transfer function.

Particularizing for the negative and positive particle, the term U_{eq} from Eq. (2a) may be expressed as in Eq. (10), taking into account that the boundary condition for the positive particle is negative if the current applied to the cell $I(s)$ is considered positive while charging:

$$U_{eq}(s) = OCP_p\left(\left[-\frac{3K_p}{\tau_p s} - \frac{K_p/5}{1 + \left(0.0207\tau_p s\right)^{0.82}}\right]I(s)\right) - OCP_n\left(\left[\frac{3K_n}{\tau_n s} + \frac{K_n/5}{1 + \left(0.0207\tau_n s\right)^{0.82}}\right]I(s)\right) \tag{10}$$

where $\tau_p = \frac{R_p^2}{D_p}$, $\tau_n = \frac{R_n^2}{D_n}$, $K_p = \frac{\tau_p}{3\epsilon_p AFL_p c_{p,max}}$ and $K_n = \frac{\tau_n}{3\epsilon_n AFL_n c_{n,max}}$.

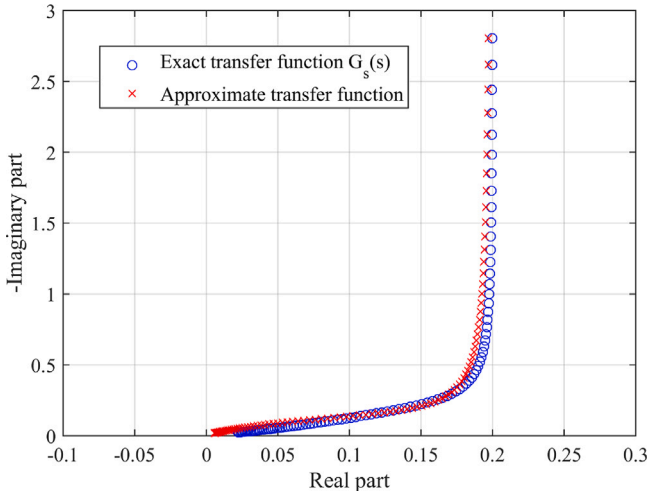

Fig. 1. Nyquist plot of the frequency response of the exact and approximate normalized transfer functions in Eq. (9) for solid diffusion. Note that the real and imaginary axes have different scales.

2.3. Electrolyte diffusion transfer function

Next, the frequency response of the η_c term in Eq. (2) must be determined in order to calculate the overpotential due to concentration gradients in the electrolyte. Consequently, the electrode-averaged lithium concentration in the electrolyte has to be evaluated. For this purpose, the diffusion process described in Eq. (11) is analyzed [14]:

$$\epsilon_{e,n}\frac{\partial c_{e,n}(x,t)}{\partial t} = \epsilon_{e,n}^{b} D_e \frac{\partial^2 c_{e,n}(x,t)}{\partial x^2} - (1-t^+)\frac{I}{AFL_n}, 0 < x < L_n \tag{11a}$$

$$\epsilon_{e,s}\frac{\partial c_{e,s}(x,t)}{\partial t} = \epsilon_{e,s}^{b} D_e \frac{\partial^2 c_{e,s}(x,t)}{\partial x^2}, L_n < x < L_n + L_s \tag{11b}$$

$$\epsilon_{e,p}\frac{\partial c_{e,p}(x,t)}{\partial t} = \epsilon_{e,p}^{b} D_e \frac{\partial^2 c_{e,p}(x,t)}{\partial x^2} - (1-t^+)\frac{I}{AFL_p}, L_n + L_s < x < L \tag{11c}$$

where D_e is the diffusion coefficient for lithium in the electrolyte, x is the linear distance along the cell length $L = L_n + L_s + L_p$, and the reference $x = 0$ is placed at the interface between the anode and the current collector. The boundary conditions at the endpoints of the cell are the following [14]:

$$\left.\frac{\partial c_{e,n}(x,t)}{\partial x}\right|_{x=0} = 0, \qquad \left.\frac{\partial c_{e,p}(x,t)}{\partial x}\right|_{x=L} = 0, \tag{12}$$

as well as continuity in concentration and flux between the different domains [14]:

$$\left.c_{e,n}(x,t)\right|_{x=L_n} = \left.c_{e,s}(x,t)\right|_{x=L_n}, \qquad \left.c_{e,s}(x,t)\right|_{x=L_n+L_s} = \left.c_{e,p}(x,t)\right|_{x=L_n+L_s}$$

$$\left.\epsilon_n^b \frac{\partial c_{e,n}(x,t)}{\partial x}\right|_{x=L_n} = \left.\epsilon_s^b \frac{\partial c_{e,s}(x,t)}{\partial x}\right|_{x=L_n}, \qquad \left.\epsilon_n^b \frac{\partial c_{e,s}(x,t)}{\partial x}\right|_{x=L_n+L_s} = \left.\epsilon_p^b \frac{\partial c_{e,p}(x,t)}{\partial x}\right|_{x=L_n+L_s} \tag{13}$$

Proceeding as in Section 2.2, the variation in concentration with respect to the typical lithium concentration in the electrolyte $c_{e,typ}$ is taken as the equation variable:

$$\tilde{c}_{e,k}(x,t) = c_{e,k}(x,t) - c_{e,typ} \tag{14}$$

Additionally, the following spatial variables are considered for convenience from now on:

$$x_n = x, x_n \in [0, L_n], \quad x_s = x - L_n, x_s \in [0, L_s], \quad x_p = L - x, x_p \in [0, L_p] \tag{15}$$

Taking the Laplace transform of Eq. (11) yields the following set of ordinary differential equations:

$$\frac{\partial^2 \tilde{c}_{e,n}(x_n,s)}{\partial x_n^2} - \frac{s}{\epsilon_{e,n}^{b-1} D_e}\tilde{c}_{e,n}(x_n,s) = \frac{(1-t^+)}{AFL_n D_e \epsilon_{e,n}^b} I(s) \tag{16a}$$

$$\frac{\partial^2 \tilde{c}_{e,s}(x_s,s)}{\partial x_s^2} - \frac{s}{\epsilon_{e,s}^{b-1} D_e}\tilde{c}_{e,s}(x_s,s) = 0 \tag{16b}$$

$$\frac{\partial^2 \tilde{c}_{e,p}(x_p,s)}{\partial x_p^2} - \frac{s}{\epsilon_{e,p}^{b-1} D_e}\tilde{c}_{e,p}(x_p,s) = \frac{(1-t^+)}{AFL_p D_e \epsilon_{e,p}^b} I(s) \tag{16c}$$

Solving Eq. (16) and applying the boundary conditions at the endpoints of the cell in Eq. (12) yields Eq. (17):

$$\tilde{c}_{e,n}(x_n,s) = 2C_n \cosh\left(x_n\sqrt{\frac{s}{\epsilon_{e,n}^{b-1} D_e}}\right) - \frac{(1-t^+)}{AFL_n\epsilon_{e,n}}\frac{I(s)}{s} \tag{17a}$$

$$\tilde{c}_{e,s}(x_s,s) = C_{s,1}\exp\left(x_s\sqrt{\frac{s}{\epsilon_{e,s}^{b-1} D_e}}\right) + C_{s,2}\exp\left(-x_s\sqrt{\frac{s}{\epsilon_{e,s}^{b-1} D_e}}\right) \tag{17b}$$

$$\tilde{c}_{e,p}(x_p,s) = 2C_p \cosh\left(x_p\sqrt{\frac{s}{\epsilon_{e,p}^{b-1} D_e}}\right) - \frac{(1-t^+)}{AFL_p\epsilon_{e,p}}\frac{I(s)}{s} \tag{17c}$$

where C_n, $C_{s,1}$, $C_{s,2}$ and C_p have to be determined from the boundary conditions in Eq. (13). In this article, instead of solving for the coefficients directly, we propose a method to simplify the system of equations in Eq. (17) by deriving the required conditions to reduce the model. It has to be noted that the consideration of spatial variables as in Eq. (15) allows for the definition of the following timescales:

$$\tau_{e,n} = \frac{L_n^2}{\epsilon_{e,n}^{b-1} D_e}, \quad \tau_{e,s} = \frac{L_s^2}{\epsilon_{e,s}^{b-1} D_e}, \quad \tau_{e,p} = \frac{L_p^2}{\epsilon_{e,p}^{b-1} D_e} \tag{18}$$

The ratio between the lithium migration timescales in the separator and the electrodes is determined by Eq. (19):

$$\frac{\tau_{e,s}}{\tau_{e,n,p}} = \frac{L_s^2 \epsilon_{e,n,p}^{b-1}}{L_{n,p}^2 \epsilon_{e,s}^{b-1}} \tag{19}$$

If this ratio is sufficiently close to 0, the electrolyte concentration in the separator may be considered to be in steady state with respect to that in the electrodes. This results in a linear concentration profile along the separator length, by taking the limit $s \to 0$ in Eq. (16b). The slope m of the concentration in the separator is determined by the boundary condition regarding flux continuity in Eq. (13):

$$m = 2C_n \frac{\epsilon_{e,n}^b}{\epsilon_{e,s}^b}\sqrt{\frac{s}{\epsilon_{e,n}^{b-1} D_e}}\sinh\left(\sqrt{\tau_{e,n}s}\right) \tag{20}$$

A further simplification is carried out by calculating the ratio between the concentration at the electrode-separator interface and the total concentration increment in the negative electrode. The concentration at the electrode-separator interface is calculated assuming that it is equal to half of the total variation in the separator:

$$\left|\tilde{c}_{e,s}|_{x_s=0}\right| = \frac{mL_s}{2} = C_n \frac{\epsilon_{e,n}^b}{\epsilon_{e,s}^b}\sqrt{\frac{sL_s^2}{\epsilon_{e,n}^{b-1} D_e}}\sinh\left(\sqrt{\tau_{e,n}s}\right) \tag{21}$$

The concentration increment in the negative electrode is calculated directly by substituting in Eq. (17a):

$$\left|\Delta\tilde{c}_{e,n}\right| = 2C_n\left[\cosh\left(\sqrt{\tau_{e,n}s}\right) - 1\right] \tag{22}$$

Therefore, the corresponding ratio is calculated as follows:

$$\left|\frac{\tilde{c}_{e,s}|_{x_s=0}}{\Delta\tilde{c}_{e,s}}\right| = \frac{1}{2}\frac{\epsilon_{e,n}^b}{\epsilon_{e,s}^b}\frac{\sinh\left(\sqrt{\tau_{e,n}s}\right)}{\cosh\left(\sqrt{\tau_{e,n}s}\right) - 1}\sqrt{\frac{sL_s^2}{D_e\epsilon_{e,n}^{b-1}}} = \frac{1}{2}\frac{\epsilon_{e,n}^b}{\epsilon_{e,s}^b}\coth\left(\frac{\sqrt{\tau_{e,n}s}}{2}\right)\sqrt{\frac{sL_s^2}{D_e\epsilon_{e,n}^{b-1}}} \tag{23}$$

One can verify that this ratio reduces to $\frac{L_s\epsilon_{e,n}^b}{L_n\epsilon_{e,s}^b}$ for the frequency range of interest around $\omega = \frac{1}{\tau_{e,n}}$. Taking this into account, if $\frac{L_s\epsilon_{e,n,p}^b}{L_{n,p}\epsilon_{e,s}^b} \ll 1$, the variations in concentration in the separator may be neglected in comparison to those in the electrodes and, as a result, the boundary condition for the concentration in the negative electrode may be approximated by $\tilde{c}_{e,n}(x_n, s)\Big|_{x_n=L_n} = 0$.

Upon applying said boundary condition, the variation in the electrolyte concentration is obtained as a function of x_n and s:

$$\tilde{c}_{e,n}(x_n, s) = \frac{(1-t^+)}{AFL_n\epsilon_{e,n}}\frac{I(s)}{s}\left[\frac{\cosh\left(x_n\sqrt{\frac{s}{\epsilon_{e,n}^{b-1}D_e}}\right)}{\cosh\left(\sqrt{\tau_{e,n}s}\right)} - 1\right] \tag{24}$$

Next, the electrode-averaged value of the variation in electrolyte concentration is calculated:

$$\begin{aligned}\overline{\tilde{c}_{e,n}(s)} &= \frac{1}{L_n}\int_0^{L_n}\tilde{c}_{e,n}(x_n, s)dx_n \\ &= \frac{(1-t^+)}{AFL_n\epsilon_{e,n}}\frac{I(s)}{s}\left[\frac{1}{\sqrt{\tau_{e,n}s}\coth\left(\sqrt{\tau_{e,n}s}\right)} - 1\right]\end{aligned} \tag{25}$$

Therefore, the transfer function from the applied current to the electrode-averaged variation in electrolyte concentration may be expressed as:

$$G_e(s) = \frac{\overline{\tilde{c}_{e,n}(s)}}{I(s)} = K_{e,n}\left[\frac{1-\sqrt{\tau_{e,n}s}\coth\left(\sqrt{\tau_{e,n}s}\right)}{\tau_{e,n}s\sqrt{\tau_{e,n}s}\coth\left(\sqrt{\tau_{e,n}s}\right)}\right] \tag{26}$$

where $K_{e,n} = \frac{(1-t^+)\tau_{e,n}}{AFL_n\epsilon_{e,n}}$.

Proceeding as in Section 2.2, one can study the behavior of $G_e(s)$ in the limits $s \to 0$ and $s \to \infty$ as in Eq. (27):

$$G_e(s) \approx \begin{cases} -\frac{K_{e,n}}{3}, & s \to 0 \\ 0, & s \to \infty \end{cases} \tag{27}$$

In order to approximate the frequency response of $G_e(s)$ between these two limits, we propose a ZARC element as expressed in Eq. (28):

$$K_{e,n}\left[\frac{1-\sqrt{\tau_{e,n}s}\coth\left(\sqrt{\tau_{e,n}s}\right)}{\tau_{e,n}s\sqrt{\tau_{e,n}s}\coth\left(\sqrt{\tau_{e,n}s}\right)}\right] \approx -\frac{K_{e,n}/3}{1+\left(\beta_e\tau_{e,n}s\right)^{\alpha_e}} \tag{28}$$

As in Section 2.2, α_e and β_e must be determined so as to obtain the closest approximation to $G_e(s)$. For this purpose, the frequency response of both transfer functions is plotted in a Nyquist diagram and the impedance error between the exact and the approximate transfer function is minimized within a range of frequencies. In this case, we have considered the interval $\omega = \left[\frac{1}{10^3\tau_{e,n}}, \frac{10^3}{\tau_{e,n}}\right]$ and the resulting values are $\alpha_e = 0.9936$ and $\beta_e = 0.3983$. The Nyquist plot of the frequency response of both transfer functions with a positive real part is shown in Fig. 2.

A similar result is obtained for the positive electrode with a plus sign. As in Section 2.2, Eq. (28) is expressed in terms of the normalized frequency $\tau_{e,n}s$, so this approximation remains valid regardless of the specific physical parameter values. In the interest of simplicity, a value of $\alpha_e = 1$ will be used further in this article. Lastly, the overpotential due to concentration gradients in the electrolyte η_c is calculated according to Eq. (2b):

$$\begin{aligned}\eta_c(s) &= \frac{2RT}{F}\frac{(1-t^+)}{c_{e,typ}}\left(\overline{c_{e,p}} - \overline{c_{e,n}}\right) \\ &= \frac{2RT}{F}\frac{(1-t^+)}{c_{e,typ}}\left(\frac{K_{e,p}/3}{1+\beta\tau_{e,p}s} + \frac{K_{e,n}/3}{1+\beta\tau_{e,n}s}\right)I(s)\end{aligned} \tag{29}$$

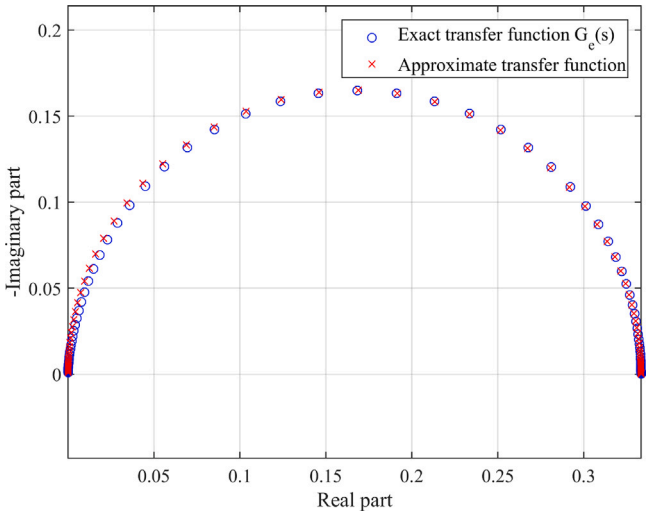

Fig. 2. Nyquist plot of the frequency response of the exact and approximate normalized transfer functions in Eq. (28) for diffusion in the electrolyte.

If $L_n \approx L_p$ and $\epsilon_{e,n} \approx \epsilon_{e,p}$, the terms corresponding to both electrodes in Eq. (29) may be combined into one single RC network.

2.4. Charge transfer overpotential

From the expressions for the solid and electrolyte concentrations determined in Sections 2.2 and 2.3, an accurate approximation of the reaction overpotentials may be obtained according to Eq. (2c). For this purpose, the exchange current densities $j_{0,n}$ and $j_{0,p}$ are calculated as follows [14]:

$$\begin{aligned}j_{0,n} &= \frac{1}{L_n}\int_0^{L_n} m_n c_{n,max}\sqrt{\chi_{s,n}(1-\chi_{s,n})}\sqrt{c_{e,n}}dx_n \\ j_{0,p} &= \frac{1}{L_p}\int_0^{L_p} m_p c_{p,max}\sqrt{\chi_{s,p}(1-\chi_{s,p})}\sqrt{c_{e,p}}dx_p\end{aligned} \tag{30}$$

where m_n and m_p are the reaction rates of the negative and positive electrode, respectively. Note that $\chi_{s,n}$ and $\chi_{s,p}$ have been determined already in Section 2.2 and do not depend on the x dimension in the SPMe. Therefore, the negative electrode exchange current density may be rewritten as follows:

$$j_{0,n} = m_n c_{n,max}\sqrt{\chi_{s,n}(1-\chi_{s,n})}\sqrt{c_{e,typ}}\frac{1}{L_n}\int_0^{L_n}\sqrt{1+\frac{\tilde{c}_{e,n}}{c_{e,typ}}}dx_n \tag{31}$$

Assuming that the variation in the electrolyte concentration is sufficiently smaller than the typical concentration $c_{e,typ}$, the following approximation can be made:

$$j_{0,n} \approx m_n c_{n,max}\sqrt{\chi_{s,n}(1-\chi_{s,n})}\sqrt{c_{e,typ}}\frac{1}{L_n}\int_0^{L_n}\left(1+\frac{\tilde{c}_{e,n}}{2c_{e,typ}}\right)dx_n \tag{32}$$

Consequently, the negative electrode exchange current density may be rewritten as a function of the electrode-averaged variation in the electrolyte concentration $\overline{\tilde{c}_{e,n}}$, which was determined in the previous Section:

$$j_{0,n} \approx m_n c_{n,max}\sqrt{\chi_{s,n}(1-\chi_{s,n})}\sqrt{c_{e,typ}}\left(1+\frac{\overline{\tilde{c}_{e,n}}}{2c_{e,typ}}\right) \tag{33}$$

From this expression of the exchange current density, the charge-transfer overpotential may be calculated according to Eq. (2c):

$$\eta_{r,n} = \frac{2RT}{F}\sinh^{-1}\left(\frac{IR_n}{6j_{0,n}\epsilon_n L_n A}\right) \tag{34}$$

This may also be expressed via the charge-transfer resistance, including its explicit dependence on the applied current as in Eq. (35)

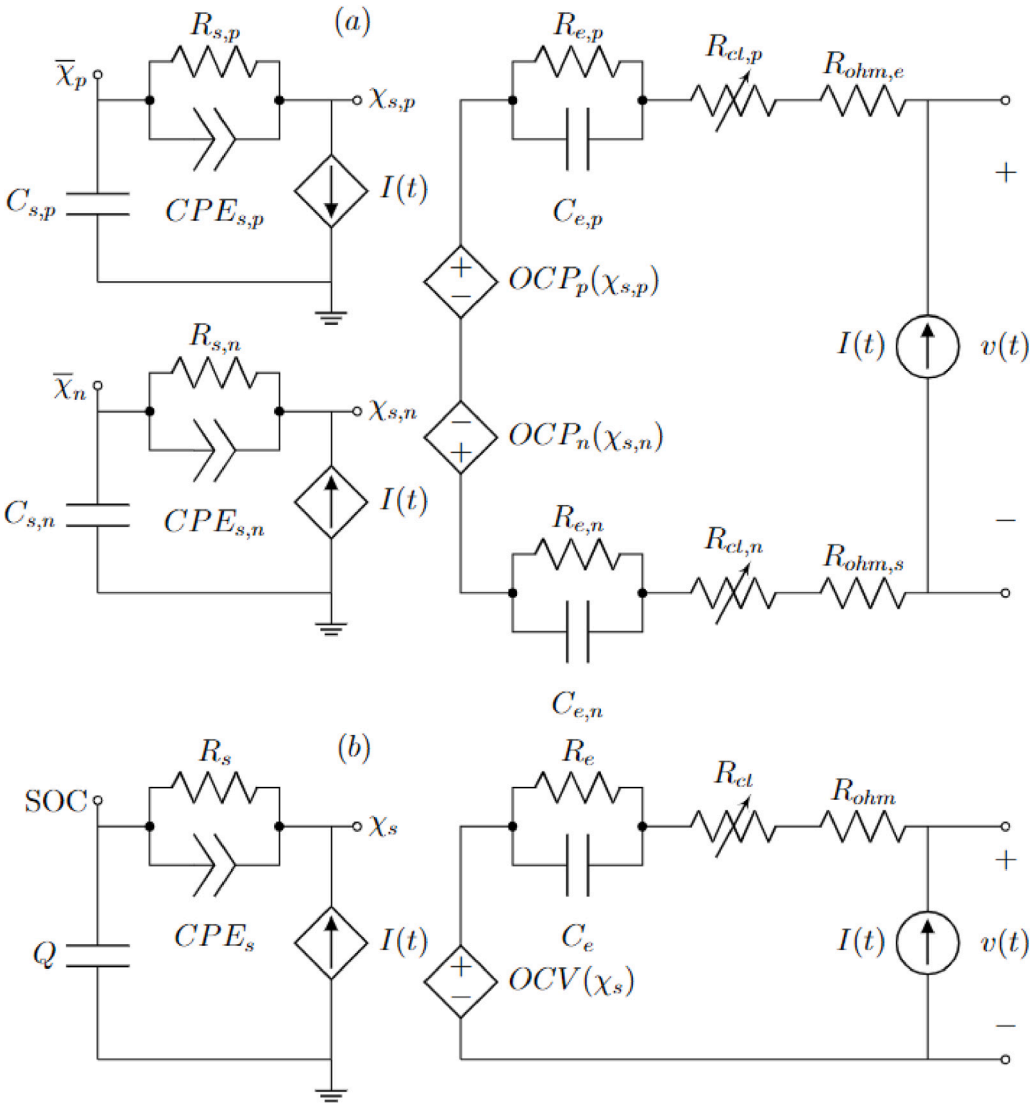

Fig. 3. (a) Full equivalent circuit model. (b) Simplified equivalent circuit model.

$$R_{ct,n}(I) = \frac{2RT}{FI_{0,n}}\left[\frac{I_{0,n}}{I}\sinh^{-1}\left(\frac{I}{I_{0,n}}\right)\right], \qquad I_{0,n} = \frac{6j_{0,n}\epsilon_n L_n A}{R_n} \tag{35}$$

A similar result is obtained for the positive electrode. We consider this to be a major advantage of employing electrode-averaged quantities as in [14], which allows for an accurate estimation of the reaction overpotential from only the electrode-averaged electrolyte concentration instead of having to solve for the concentration profile along the x dimension. Taking into account the current dependence of the reaction overpotentials is especially critical in applications where a wide range of current rates is expected.

2.5. Equivalent circuit model

According to the output voltage expression in Eq. (1) and the resulting equations for the individual terms in Eq. (2), the equivalent circuit model in Fig. 3-(a) may be constructed, where the resistors $R_{ohm,e} = \frac{1}{\kappa A}\left(\frac{L_n}{3\epsilon_{e,n}^b} + \frac{L_s}{\epsilon_{e,s}^b} + \frac{L_p}{3\epsilon_{e,p}^b}\right)$ and $R_{ohm,s} = \frac{1}{3A}\left(\frac{L_n}{\sigma_n} + \frac{L_p}{\sigma_p}\right)$ correspond to the terms in Eqs. (2d) and (2e).

For the time-domain implementation of the circuit, a set of serially connected parallel RC branches will be employed as an approximation of the ZARC element. In particular, we will use the continuous approximation by 7 RC elements that we presented in [53]. This approach is the most appropriate for the time-domain simulation of the ZARC element as we showed in [56], due to the fact that it avoids the issues caused by the specification of a memory length in the Grünwald–Letnikov approach. Taking the fractional order α, the resistor R_{ZARC} and the time constant τ_{ZARC} as inputs, the parameter values are directly calculated as $R_i = R_{ZARC} \cdot r_i(\alpha)$ and $\tau_i = \tau_{ZARC} \cdot t_i(\alpha)$ for seven-element network according to Table 1 [53]:

Table 1
Parameter equations for the 7-RC approximation as a function of α [53].

Parameter	Expression
$r_1 = r_7$	$0.14(1-\alpha)^2$
$r_2 = r_6$	$0.22(1-\alpha) - 0.08(1-\alpha)^3$
$r_3 = r_5$	$\left(0.12 + 0.057e^{3.4\alpha}\right)(1-\alpha)$
r_4	$1 - 2\left(r_1 + r_2 + r_3\right)$
$t_1 = 1/t_7$	$1.4 \cdot 10^{-8} e^{19\alpha(1.6-\alpha)}$
$t_2 = 1/t_6$	$\frac{0.078\alpha^{5.63}}{0.026+\alpha^{3.67}}$
$t_3 = 1/t_5$	$\frac{0.56\alpha^{2.27}}{0.4+\alpha^{1.3}}$
t_4	1

As a result, the approximate discrete state-space representation of a ZARC element is shown in Eq. (36):

$$\begin{aligned} x_{ZARC}(k) &= \begin{bmatrix} i_1(k) & i_2(k) & \dots & i_7(k) \end{bmatrix}^T \\ x_{ZARC}(k) &= A_{ZARC}x_{ZARC}(k-1) + B_{ZARC}u(k-1) \\ y_{ZARC}(k) &= C_{ZARC}x_{ZARC}(k) \end{aligned} \tag{36}$$

where x_{ZARC} is the state vector, u is the input current and y_{ZARC} is the total voltage difference in the subcircuit, with the following state-space representation matrices:

$$\begin{aligned} A_{ZARC} &= diag\left[\exp\left(-\tfrac{\Delta t}{\tau_1}\right) \quad \exp\left(-\tfrac{\Delta t}{\tau_2}\right) \quad \dots \quad \exp\left(-\tfrac{\Delta t}{\tau_7}\right)\right] \\ B_{ZARC} &= \left[1-\exp\left(-\tfrac{\Delta t}{\tau_1}\right) \quad 1-\exp\left(-\tfrac{\Delta t}{\tau_2}\right) \quad \dots \quad 1-\exp\left(-\tfrac{\Delta t}{\tau_7}\right)\right]^T \\ C_{ZARC} &= \begin{bmatrix} R_1 & R_2 & \dots & R_7 \end{bmatrix} \end{aligned} \tag{37}$$

where Δt is the sampling time.

Consequently, the state vector and the state equation of the ECM are as follows:

$$\begin{aligned} x(k) &= \left[\overline{\chi}_p(k) \quad x_{ZARC,p}(k) \quad \overline{\tilde{c}_{e,p}(k)} \quad \overline{\chi}_n(k) \quad x_{ZARC,n}(k) \quad \overline{\tilde{c}_{e,n}(k)}\right]^T \\ x(k) &= Ax(k-1) + Bu(k-1), \qquad u(k) = I(k) \end{aligned} \tag{38}$$

where

$$A = diag\left[1 \quad diag(A_{ZARC,p}) \quad \exp\left(-\tfrac{\Delta t}{\beta_e \tau_{e,p}}\right) \quad 1 \quad diag(A_{ZARC,n}) \quad \exp\left(-\tfrac{\Delta t}{\beta_e \tau_{e,n}}\right)\right]$$

$$B = \begin{bmatrix} -\frac{K_p \Delta t}{3\tau_p} \\ -B_{ZARC,p} \\ \frac{K_{e,p}}{3}\left[1-\exp\left(-\frac{\Delta t}{\beta_e \tau_{e,p}}\right)\right] \\ \frac{K_n \Delta t}{3\tau_n} \\ B_{ZARC,n} \\ -\frac{K_{e,n}}{3}\left[1-\exp\left(-\frac{\Delta t}{\beta_e \tau_{e,n}}\right)\right] \end{bmatrix} \tag{39}$$

Note the minus sign in the terms corresponding to the positive particle and the electrolyte concentration in the negative electrode in matrix B. Before evaluating the output voltage expression, it is convenient to calculate explicitly the surface concentration of both particles as well as the exchange current density in both electrodes:

$$\begin{aligned} \chi_{s,p}(k) &= \overline{\chi}_p(k) + C_{ZARC,p}x_{ZARC,p}(k) \\ \chi_{s,n}(k) &= \overline{\chi}_n(k) + C_{ZARC,n}x_{ZARC,n}(k) \\ j_{0,p}(k) &= m_p c_{p,max}\sqrt{\chi_{s,p}(k)(1-\chi_{s,p}(k))}\sqrt{c_{e,typ}}\left(1+\frac{\overline{\tilde{c}_{e,p}(k)}}{2c_{e,typ}}\right) \\ j_{0,n}(k) &= m_n c_{n,max}\sqrt{\chi_{s,n}(k)(1-\chi_{s,n}(k))}\sqrt{c_{e,typ}}\left(1+\frac{\overline{\tilde{c}_{e,n}(k)}}{2c_{e,typ}}\right) \end{aligned} \tag{40}$$

Taking all the previous equations into account, the output voltage expression is as follows:

$$\begin{aligned} v(k) = {} & OCP_p(\chi_{s,p}(k)) - OCP_n(\chi_{s,n}(k)) + \frac{2RT}{F}\frac{(1-t^+)}{c_{e,typ}}\left(\overline{c_{e,p}(k)} - \overline{c_{e,n}(k)}\right) \\ & + \frac{2RT}{F}\left[\sinh^{-1}\left(\frac{IR_p}{6j_{0,p}(k)\epsilon_p L_p A}\right) + \sinh^{-1}\left(\frac{IR_n}{6j_{0,n}(k)\epsilon_n L_n A}\right)\right] \\ & + \frac{I}{\kappa A}\left(\frac{L_n}{3\epsilon_{e,n}^b} + \frac{L_s}{\epsilon_{e,s}^b} + \frac{L_p}{3\epsilon_{e,p}^b}\right) \\ & + \frac{I}{3A}\left(\frac{L_n}{\sigma_n} + \frac{L_p}{\sigma_p}\right) \end{aligned} \tag{41}$$

If both electrodes are assumed to have similar physical and spatial properties, the ECM can be further simplified to that in Fig. 3-(b), thus reducing in half the number of required states.

The developed ECM may be interpreted as the combination of the two discussed approaches in Section 1: on the one hand, the transcendental transfer functions are obtained directly from the electrochemical model and then approximated with fractional-order transfer functions instead of Padé's approximant [40–43] in our case. On the other hand, the standard RC equivalent circuit model from [36] is split into two sections as in [39], so that the leftmost one accounts for the lithium diffusion within the active material particles. Consequently, the lithium concentration is evaluated at their surface, thus establishing a more accurate correspondence with the manner in which the electrode potential is calculated in electrochemical models. However, a better description of the diffusion process is achieved with a ZARC element instead of a RC network, as indicated by the optimal order exponent $\alpha = 0.82$. Therefore, this model, stated in this way, may be useful for most of the applications where ECMs are employed providing additional physical insight, and may also be implemented in standard circuit simulators by substituting the ZARC element by its multiple-RC approximation [53], thus allowing for a simple simulation of constant-voltage phases by substituting the current source in Fig. 3 by a voltage source.

2.6. Frequency domain application

From the obtained transfer functions, it is possible to determine the medium and low frequency response of the cell directly given its physical parameters. However, the high-frequency transient effects of the charge transfer processes are usually not considered in the DFN or SPMe due to them being orders of magnitude faster than diffusion dynamics. Consequently, in order to accurately reproduce EIS data, a CPE is usually connected in parallel with the charge-transfer resistance R_{ct} in the circuit shown in Fig. 3-(b). The small-signal value of R_{ct} is calculated by taking into account that for small values of x, $x^{-1}\sinh^{-1}(x) \approx 1$:

$$R_{ct}(I \approx 0) = \frac{2RT}{FI_0}, \qquad Z_{ct}(s) = \frac{R_{ct}}{1+(\tau_{ct}s)^{\alpha_{ct}}} \tag{42}$$

Conversely, if the frequency-domain behavior of the battery cell is characterized experimentally in an EIS test, there will be a substantial overlap between the effects of both electrodes and only the effective parameters for the simplified ECM in Fig. 3-(b) will be identifiable. Given that an EIS test consists of small-signal variations around a certain operating point, the ECM is linearized around $SOC = SOC_{EIS}$. Using the fact that cell SOC remains unchanged, one can write:

$$OCV(\chi_s) = OCV(SOC_{EIS}) + \left.\frac{\partial OCV}{\partial SOC}\right|_{SOC_{EIS}}\tilde{\chi}_s \tag{43}$$

where $\left.\frac{\partial OCV}{\partial SOC}\right|_{SOC_{EIS}}$ is determined empirically from the OCV-SOC relationship and the frequency response of $\tilde{\chi}_s$ may be approximated by that of a ZARC element. Therefore, a possible transfer function for fitting EIS data is composed of the addition of an ohmic resistor, a high-frequency ZARC element for charge transfer processes, a mid-frequency RC element for the diffusion in the electrolyte and a low-frequency ZARC element for the solid diffusion, as shown in Eq. (44):

$$Z(s) = R_{ohm} + \frac{R_{ct}}{1+(\tau_{ct}s)^{\alpha_{ct}}} + \frac{R_e}{1+\tau_e s} + \left.\frac{\partial OCV}{\partial SOC}\right|_{SOC_{EIS}}\frac{K_s}{1+(\tau_s s)^{\alpha_s}} \tag{44}$$

where and the parameters to be identified are R_{ohm}, R_{ct}, τ_{ct}, α_{ct}, R_e, τ_e, K_s and τ_s, although τ_{ct} and α_{ct} will not be used in the ECM. Additionally, the value of the exchange current I_0 may be calculated directly from R_{ct}, so as to take into account the current dependence of the charge transfer resistance for large-signal operation.

We believe that the correspondence between the time and frequency-domain behaviors of the cell is an advantage over electrochemical models, as it also provides a consistent characterization method since physical parameters are grouped in resistors and time constants.

Table 2
Parameter set from [14].

Parameter	Units	Description	Value
Negative electrode			
L_n	m	Thickness	$1 \cdot 10^{-4}$
R_n	m	Particle radius	$1 \cdot 10^{-5}$
D_n	m^2/s	Solid diffusivity	$3.9 \cdot 10^{-14}$
ϵ_n	–	Active material volume fraction	0.6
$c_{n,max}$	mol/m^3	Maximum lithium concentration	$2.4983 \cdot 10^4$
σ_n	S/m	Solid conductivity	100
$\epsilon_{e,n}$	–	Porosity	0.3
m_n	$(A/m^2)(m^3/mol)^{1.5}$	Reaction rate	$2 \cdot 10^{-5}$
Positive electrode			
L_p	m	Thickness	$1 \cdot 10^{-4}$
R_p	m	Particle radius	$1 \cdot 10^{-5}$
D_p	m^2/s	Solid diffusivity	$1 \cdot 10^{-13}$
ϵ_p	–	Active material volume fraction	0.5
$c_{p,max}$	mol/m^3	Maximum lithium concentration	$5.1218 \cdot 10^4$
σ_p	S/m	Solid conductivity	10
$\epsilon_{e,p}$	–	Porosity	0.3
m_p	$(A/m^2)(m^3/mol)^{1.5}$	Reaction rate	$6 \cdot 10^{-7}$
Separator			
L_s	m	Thickness	$2.5 \cdot 10^{-5}$
$\epsilon_{e,s}$	–	Porosity	1
Overall			
$c_{e,typ}$	mol/m^3	Typical electrolyte concentration	$1 \cdot 10^3$
D_e	m^2/s	Typical electrolyte diffusivity	$5.34 \cdot 10^{-10}$
κ	S/m	Typical electrolyte conductivity	1.1
t^+	–	Transference number	0.4
b	–	Bruggeman coefficient	1.5
A	m^2	Electrode area	$2.8359 \cdot 10^{-2}$
Q	Ah	Cell capacity	0.68

3. Theoretical results and discussion

In this section, the performance of the proposed ECM is validated against the SPMe from [14] for different current profiles. For the simulation of the electrochemical model, we have used PyBaMM (Python Battery Mathematical Modeling) [57]. PyBaMM is a battery modeling software implemented in Python designed to simplify the comparison of standard battery models by providing an interface to discretization methods and numerical solvers. In this case, we have employed a typical discretization consisting of 20 points in each domain as well as 20 points for both particles.

The set of physical parameters is shown in Table 2.

Before carrying out the simulations, the validity of the approximations derived in Section 2.3 is verified:

$$\frac{L_s^2 \epsilon_{e,n,p}^{b-1}}{L_{n,p}^2 \epsilon_{e,s}^{b-1}} = 0.034 \ll 1, \qquad \frac{L_s \epsilon_{e,n,p}^{b}}{L_{n,p} \epsilon_{e,s}^{b}} = 0.041 \ll 1 \tag{45}$$

Next, the performance of the proposed ECM has been validated against the cited SPMe model by comparing their simulation results for distinct operation scenarios. In this case, we have employed four constant-current discharges at 2C, 1C, C/2 and C/5 followed by a 30-min rest where C-rate is the measurement of the charge and discharge current with respect to its nominal capacity. Additionally, we have also considered a driving cycle (US06) in order to test our model under dynamic operating conditions.

The simulation results for the constant-current discharges are shown in Fig. 4, plotted with respect to normalized time as a function of the C-rate. It is observed that the proposed model is able to reproduce the cell voltage accurately during the discharge regardless of the current rate. We attribute this mainly to the precise calculation of the charge-transfer reaction overpotentials as detailed in Section 2.4, which present a highly nonlinear dependency on current. Furthermore, the relaxation profile is also accurately modeled due to the introduction of fractional-order circuit elements to account for the solid diffusion process. The voltage response of the battery and the US06 current profile are shown in Fig. 5. It can also be observed that the proposed ECM is able to yield a greatly accurate terminal voltage in dynamic conditions. Furthermore, the comparison between the battery internal states and their equivalent in the proposed ECM is shown in Fig. 6. Given that the proposed model has been analytically derived from the SPMe, it is able to provide information about the internal states of the battery. We believe this is a qualitative advantage over standard equivalent circuit models [26], which are constructed to reproduce battery voltage only. Nevertheless, a thorough comparison between the accuracy of different ECMs with respect to experimental data constitutes a separate study that is beyond the scope of this article. There could be many factors involved in the discrepancies between model results and experimental data, such as temperature, hysteresis and current-rate effects, as well as the parameterization process and the operating conditions under which the models are tested.

The error results between the SPMe and the proposed ECM are summarized in Table 3. It has to be pointed out that not only does the model provide an accurate approximation of the terminal voltage, but also the internal states of the battery, namely the surface concentration of the solid particles and the electrode-averaged electrolyte concentration, which results in a precise calculation of the charge-transfer reaction overpotentials. The maximum voltage error occurs immediately after the end of the discharge, due to the fact that the proposed approximation for the solid diffusion transfer function is less accurate at higher frequencies, as observed in Fig. 1. This also explains the slightly higher error in the surface concentration of the negative particle in comparison to the positive particle, given its larger solid diffusion time constant. The electrode-averaged electrolyte concentration is also modeled with great accuracy: taking into account that its typical concentration is $c_{e,typ} = 1000\ mol/m^3$, the relative RMS and maximum errors are below 0.6% and 3% respectively. Note that the results for the electrolyte concentration are equal in both electrodes due to the fact that their thickness and porosity have the same values in this parameter set; this is not a general result nonetheless. In conclusion, the proposed ECM is able to accurately model the output voltage as well as the internal states with respect to an SPMe.

Lastly, a comparison on the computational requirements of both models is carried out. We have determined that the proposed ECM is about 3 to 4 times quicker on average for the same timestep and simulation profile; however, we believe that the main advantage of our model with respect to the SPMe is the number of states required. For a typical discretization, such as the one considered here, 100 states must be stored and updated every timestep for the SPMe, whereas only 18 are necessary for the full ECM and 9 for the simplified version if the 7-RC approximation of the ZARC element is employed. Nevertheless, other continuous approximations by 5 [53] and 3 [49] RC networks have also been reported in recent literature, so should the available memory be tightly constrained, the number of necessary states may be potentially reduced to 14 or 10 for the full ECM and 7 or 5 for the simplified ECM, without a major loss of accuracy. This is a crucial feature given the limitations on memory and computation power in on-board BMSs.

Furthermore, although some state observers have been proposed for the SPM and SPMe [15,42], employing an ECM makes it simpler to implement a Dual Fractional-Order Extended Kalman Filter for the concurrent estimation of state of charge and circuit parameters, as we presented in [56], with the advantage that the identified parameters are directly related to their physical counterparts in this model.

4. Experimental application

In this section, the simplified version of the proposed equivalent circuit model is compared to experimental data by identifying the equivalent circuit parameters from an EIS test.

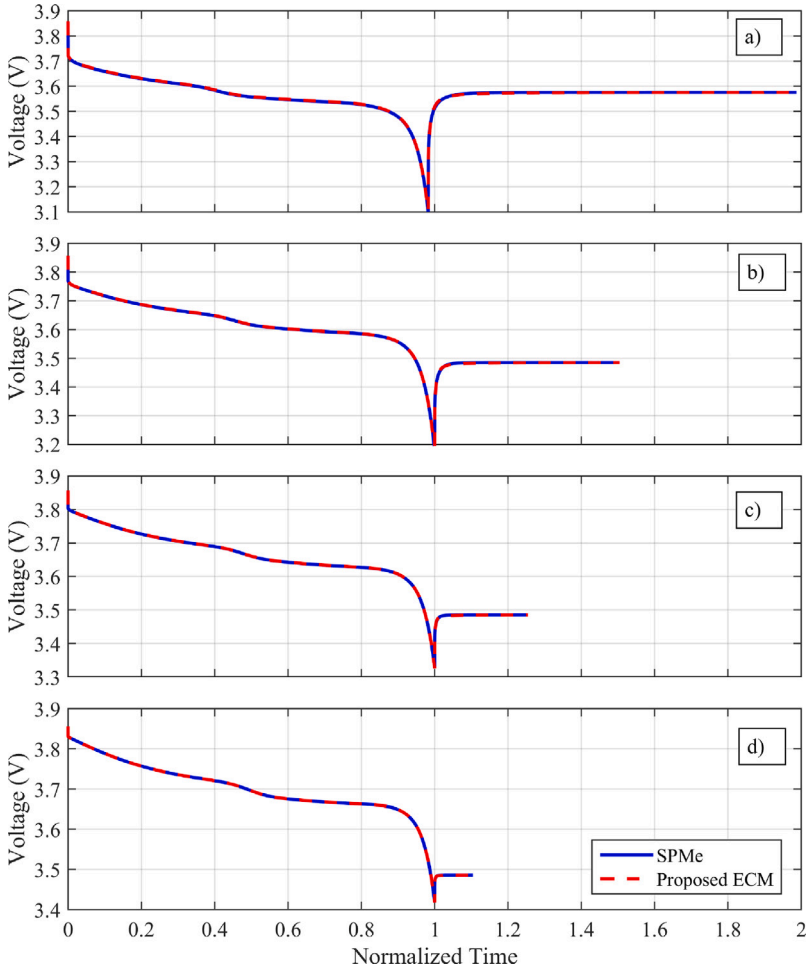

Fig. 4. Terminal voltage for the SPMe and the proposed ECM for a constant-current discharge at (a) 2C, (b) 1C, (c) C/2 and (d) C/5 respectively, followed by a 30-min rest. Curves have been plotted with respect to normalized time, i.e. time divided by the nominal discharge duration according to the C-rate.

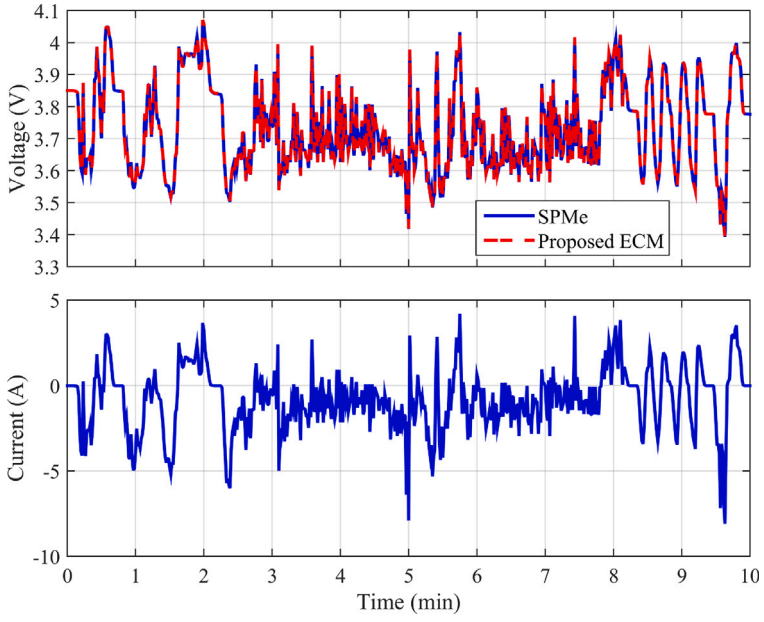

Fig. 5. Terminal voltage and input current for the SPMe and the proposed ECM for the US06 driving cycle.

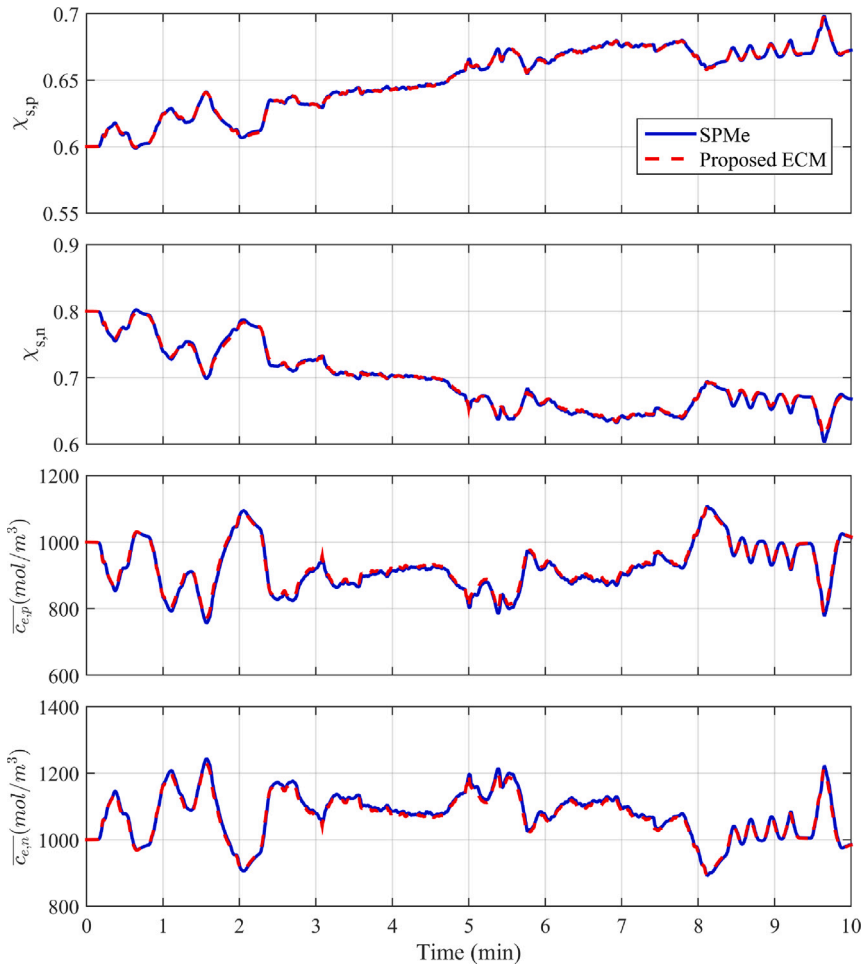

Fig. 6. Normalized surface concentration in the positive and negative particles $\chi_{s,p}, \chi_{s,p}$, and electrode-averaged electrolyte concentrations $\overline{c_{e,p}}, \overline{c_{e,n}}$ for the SPMe and the proposed ECM for the US06 driving cycle.

Table 3
RMS error results for the simulated profiles in the indicated units, with maximum error between brackets.

	2C	1C	C/2	C/5	US06
V (mV)	1.46 [15.4]	0.95 [6.24]	0.40 [2.35]	0.13 [0.77]	1.08 [3.49]
$\chi_{s,p}$ (%)	0.01 [0.04]	0.006 [0.02]	0.003 [0.01]	0.001 [0.004]	0.07 [0.41]
$\chi_{s,n}$ (%)	0.09 [0.22]	0.04 [0.11]	0.02 [0.06]	0.004 [0.02]	0.28 [1.15]
$\overline{c_{e,p}}$ (mol/m^3)	5.94 [12.3]	3.45 [5.95]	1.89 [2.97]	0.81 [1.19]	5.99 [29.6]
$\overline{c_{e,n}}$ (mol/m^3)	5.94 [12.3]	3.45 [5.95]	1.89 [2.97]	0.81 [1.19]	5.99 [29.6]
η_p (mV)	0.26 [0.42]	0.11 [0.13]	0.04 [0.49]	0.008 [0.011]	0.32 [1.40]
η_n (mV)	0.009 [0.04]	0.006 [0.011]	0.002 [0.003]	0.001 [0.001]	0.05 [0.38]

4.1. Experimental setup

In this article, a NMC811/Gr commercial cell manufactured by Samsung-SDI (INR18650-25R8) was investigated. This cell presents a nominal voltage of 3.7 V and a nominal discharge capacity Q ≥ 2500 mAh when discharged at C/5 within the upper and lower voltage limits of 4.2 V and 2.5 V, respectively. A high-precision Arbin LBT21084MC battery tester was employed for the experimental cycling schemes, whereas a Gamry Reference 3000™ potentiostat/galvanostat was used for EIS characterization. A constant ambient temperature of 23 °C was achieved with the aid of a Memmert environmental chamber. The temperatures in the environmental chamber and the cell case were measured with respective T-type copper-constantan thermocouples with a standard tolerance of ±1 °C and logged into the Arbin system. A general perspective of the battery testing system with its associated environmental chamber is shown in Fig. 7-(a), whereas a detail of the analyzed cell with its thermocouple and battery holder may be observed in Fig. 7-(b).

The experiments started with the conditioning procedures followed by added thermodynamic testing at C/25, with the purpose of determining of the Open Circuit Voltage (OCV) as a function of SOC [58]. Subsequently, a Reference Performance Test (RPT) was conducted, which consisted of a set of charge and discharge cycles at 1C, C/2 and C/5, while maintaining a CC-CV charging scheme at C/2 (1.25 A) up to 4.2 V until the current fell below to C/50 (50 mA). To conclude the RPT, an EIS test was performed at 50% SOC from 10 mHz to 10 kHz.

Once the RPT was completed, several cycles consisting of Dynamic Stress Tests (DST) profiles [59] were carried out in order to evaluate the dynamic behavior of the proposed model. The DST schedule was scaled to 700 W/kg, and repeated until the cell reached the discharge cut-off voltage.

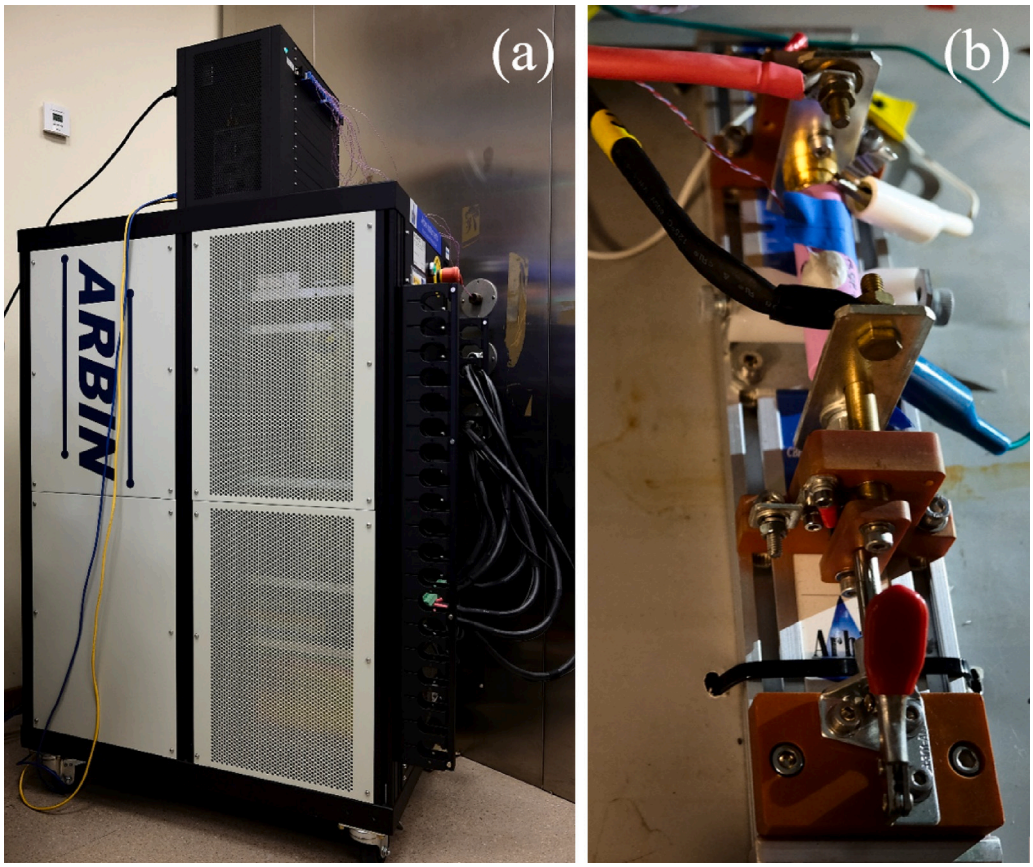

Fig. 7. (a) Arbin LBT20084 battery system and environmental chamber (b) Cell under test in the Arbin battery holder inside the climatic chamber, with its thermocouple attached with adhesive putty.

4.2. Experimental results and discussion

The purpose of this subsection is to make use of the equivalence between the frequency and time-domain behaviors of the proposed model via the obtained transfer functions. We believe this constitutes another qualitative advantage over standard circuit models due to the fact that small-signal parameters may be employed in the time domain, thus avoiding the issues with parameterizations from time-domain data. For instance, time-domain parameterizations might not be unique since there may potentially be multiple error minima with substantially different parameter values for a given current profile. We reviewed and discussed this subject in [56] and emphasized the importance of frequency-domain data for a physics-informed parameterization, as the timescales of the different processes taking place during battery operation are more easily distinguishable in EIS measurements. Nevertheless, we will not carry out a comprehensive cell parameterization as in [60] or the subsequent quantitative validation of the full model in Fig. 3-(a), since testing the complete ECM by taking into account the different characteristics of both electrodes is beyond the scope of this article.

Herein, the equivalent circuit parameters for the simplified version of the ECM in Fig. 3-(b) will be identified according to the procedure described in Section 2.6, from the EIS data obtained with the experimental scheme described in Section 4. We are aware of the fact that some parameters, such as the charge-transfer resistance, may change significantly with temperature and state of charge, as shown in Section 2. However, we will consider the reference parameters to be those identified at 50% SOC, so as to use a unique value within the whole SOC range. Furthermore, in order to avoid issues with hysteresis voltage, we will consider the discharge curve obtained at C/25 as the reference OCV given that we will only compare discharge processes. This results in $\frac{\partial OCV}{\partial SOC} \approx 0.934$ V at 50% SOC.

The identification of parameters was performed with standard Particle Swarm Optimization (PSO) [61]. The cost function was defined as the weighted distance between the experimental data and the theoretical impedance in Eq. (44) the Nyquist diagram, expressed in Eq. (46):

$$C = \sum_{k=1}^{N} w_k \Big[\big(Im(Z_{est}(j\omega_k)) - Im(Z_{exp}(j\omega_k)) \big)^2 + \big(Re(Z_{est}(j\omega_k)) - Re(Z_{exp}(j\omega_k)) \big)^2 \Big] \tag{46}$$

Although we are employing a metaheuristic optimization algorithm for parameter identification, we believe this entails an advantage over time-domain identification, since in this case the target transfer function is well defined and the upper and lower bounds for each parameter are roughly known from physical parameters. In addition to this, the determination of the parameters relative to the charge-transfer ZARC element can be carried out analytically, as we presented in [56], thus reducing the number of free parameters and the computation time as a consequence.

Experimental data and fitted results are shown in Fig. 8. The accurate match between both sets of points serves to validate the approximate transfer functions derived in Section 2.5. The minor discrepancies observed at high frequencies are not due to a modeling error, but the influence of parasitic inductive elements [45].

The value of K_s is calculated directly from R_s and $\frac{\partial OCV}{\partial SOC}$. It is also noted that τ_{Rct} has a value on the order of 1 ms, which explains why τ_{Rct} and α_{Rct} have been considered in the fit but not taken into account in time-domain simulations. Next, the identified parameters will be employed to simulate the ECM in the time domain so as to compare its behavior to the experimental data acquired according to the procedures described in Section 4.1. The obtained small-signal

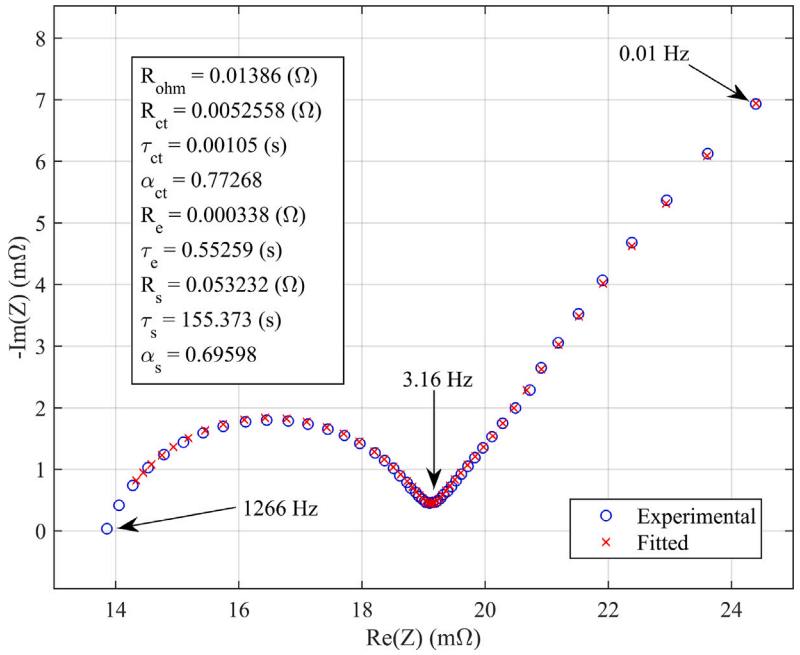

Fig. 8. Experimental EIS data at 50% SOC for the analyzed cell and fit results.

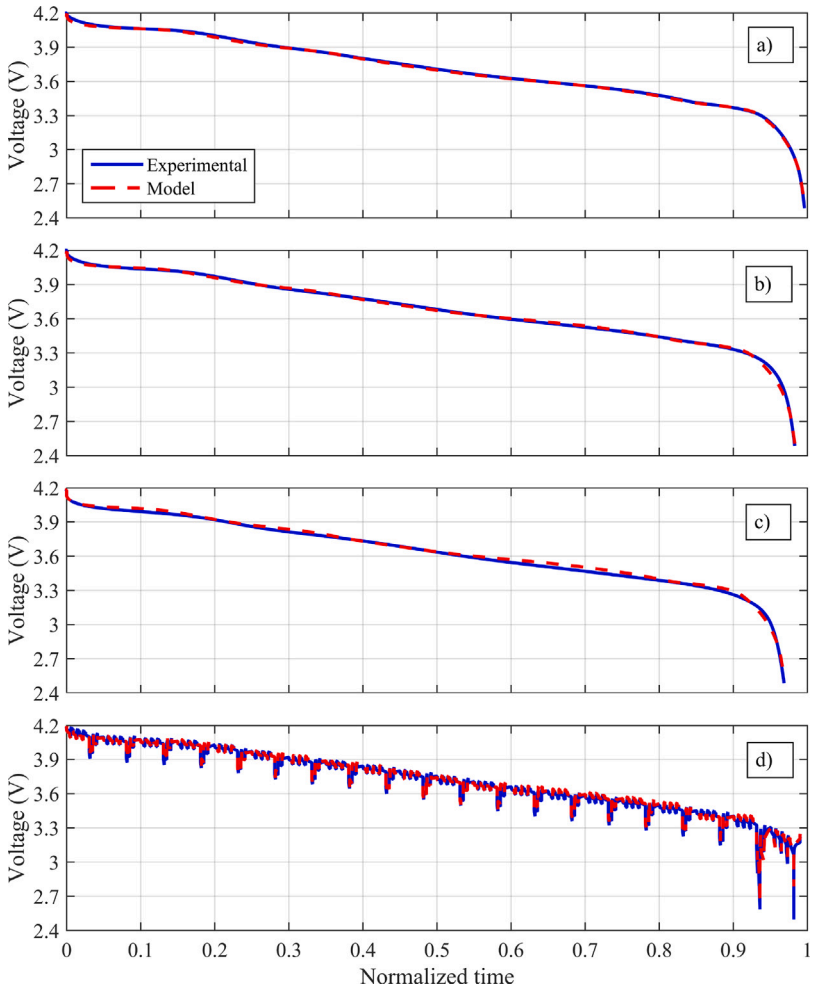

Fig. 9. Experimental and simulation results for a constant-current discharge at (a) C/5, (b) C/2 and (c) 1C and (d) a full discharge with a DST profile. Curves have been plotted with respect to normalized time, i.e. time divided by the nominal discharge duration according to the C-rate. The average discharge rate for the DST profile is C/2.

parameters may be considered as a reliable starting point; however, slight adjustments are required as a function of the current rate in order to achieve a closer agreement with experimental results. Consequently, additional nonlinear effects that are usually not considered in standard electrochemical models may be accounted for in this manner.

Simulated and experimental results are shown in Fig. 9 for C/5, C/2 and 1C discharges, along with a complete discharge following the DST profile. The curves corresponding to the model results have been obtained by tweaking the value of the resistor associated with the solid diffusion process, which is equivalent to an adjustment of effective solid diffusion coefficient. The corresponding values are $K_s = 0.045(1/A)$, $K_s = 0.029(1/A)$, $K_s = 0.020(1/A)$ and $K_s = 0.026(1/A)$, and the RMS voltage errors are 10.5 mV, 25.2 mV, 26.7 mV and 36.4 mV for the C/5, C/2, 1C and DST discharges, respectively. A decreasing dependency of this parameter on the current rate is observed from its small-signal value identified in EIS tests $K_s = 0.057(1/A)$ to that of larger average currents. It has to be pointed out that the value obtained for the defined DST profile is similar to that of the C/2 discharge, given that the former presents an average discharge rate of C/2. Nevertheless, a thorough analysis of the dependency of the effective solid diffusion coefficient with current rate is beyond the scope of this paper, and will be considered in future research.

The disagreement between the experimental and simulated results towards the end of the discharge process, especially at higher currents, may be ascribed mainly to the fact that the OCV-SOC curve is highly nonlinear at low SOCs. Therefore, the model result obtained with first-order models, such as the SPMe or this ECM, differs from that of the numerical resolution of the DFN, as demonstrated in [14]. Furthermore, we believe that the discrepancies between model and experimental results may be partially attributed to the fact that we have used the simplified ECM with representative parameters for both electrodes at large. Although we consider that the possibility to parameterize the model from frequency-domain data constitutes a qualitative advantage over standard ECMs, additional accuracy would be gained if the complete ECM accounting for both electrodes were employed instead, albeit at the expense of a significantly more complex parameterization process.

Nevertheless, we understand that the simplified version is accurate enough for many practical applications if used in conjunction with a Dual Fractional-Order Extended Kalman Filter [56], so as to simultaneously estimate SOC and circuit parameters as well as mitigate the inaccuracies that we discussed above. Moreover, an equivalent circuit formulation makes it simpler to incorporate more complex effects into the model. For instance, SOC-varying hysteresis, which is present in many battery cells, may easily be added as a circuit element as described in [20].

5. Conclusions

In this article, a fractional-order equivalent circuit model has been developed directly from the SPMe by obtaining approximate transfer functions corresponding to the solid and electrolyte diffusion, as well as the criteria for their validity. Next, the equivalence between their frequency response and circuit components is established via ZARC elements. Furthermore, a precise approximation of the reaction overpotentials is also derived as a function of the previously calculated concentrations. The proposed ECM is able to accurately replicate the theoretical behavior of the SPMe model, providing an RMS error below 1.46 mV for cell voltage, 0.28% for the surface concentration in the active material particles, 0.6% for the electrode-averaged electrolyte concentration and 0.32 mV for the charge-transfer overpotentials. Afterwards, the model is validated against experimental data by first identifying the equivalent circuit parameters from an EIS test and using them in a simplified version of the model. We believe the presented model constitutes an interesting alternative to standard ECMs because of its additional insight into internal states and correlation with physical parameters; whereas it also presents a reduced computational complexity and a simpler parameterization with respect to electrochemical models.

Table A.4
Abbreviations.

Abbreviation	Description
BMS	Battery Management System
CC-CV	Constant Current - Constant Voltage
CPE	Constant-Phase Element
DFN	Doyle–Fuller–Newman
DST	Dynamic Stress Test
DTRA	Discrete Time Realization Algorithm
ECM	Equivalent Circuit Model
EIS	Electrochemical Impedance Spectroscopy
Gr	Graphite
NMC811	Nickel–Manganese–Cobalt (811)
OCP	Open Circuit Potential
OCV	Open Circuit Voltage
SPM	Single-Particle Model
PDE	Partial Differential Equation
RMS	Root Mean Square
RPT	Reference Performance Test
SOC	State Of Charge

CRediT authorship contribution statement

Pablo Rodríguez-Iturriaga: Conceptualization, Methodology, Investigation, Writing – original draft. **David Anseán:** Investigation, Resources, Data curation, Writing – original draft. **Salvador Rodríguez-Bolívar:** Conceptualization, Methodology, Investigation, Writing – original draft, Writing – review & editing. **Manuela González:** Investigation, Resources, Data curation, Supervision. **Juan Carlos Viera:** Investigation, Resources, Data curation, Supervision. **Juan Antonio López-Villanueva:** Methodology, Investigation, Writing – review & editing, Supervision.

Declaration of competing interest

The authors declare that they have no known competing financial interests or personal relationships that could have appeared to influence the work reported in this paper.

Data availability

Data will be made available on request.

Acknowledgments

This work was partially supported by the Regional Government of Andalusia under project P18-RT-3303 from Plan Andaluz de Investigación, Desarrollo e Innovación (PAIDI 2020), by the Spanish Ministry of Science and Innovation and by FEDER funds via Project MCI-20-PID2019-110955RB-I00, by the Principality of Asturias via project AYUD/2021/50994, and by the FPU-UGR-Banco Santander Program for Predoctoral Scholarships.

Funding for open access charge: Universidad de Granada / CBUA

Appendix A. Abbreviations

See Table A.4.

Appendix B. Nomenclature

Subscripts n, s, p, e stand for negative, separator, positive and electrolyte, respectively. A tilde (as in $\tilde{c}_e$) denotes variations with respect to the initial/typical value, whereas an overline (as in $\overline{c_{e,n}}$) indicates an electrode-averaged quantity (see Table B.5).

Table B.5
Nomenclature.

Symbol	Description (Units)
$L_{n/s/p}$	Electrode/Separator thickness (m)
$R_{n/p}$	Active material particle radius (m)
$D_{n/p}$	Solid diffusivity (m^2/s)
$\epsilon_{n/p}$	Active material volume fraction in electrode
$c_{n/p,max}$	Maximum lithium concentration in active material particle (mol/m^3)
$\sigma_{n/p}$	Electrode conductivity (S/m)
$\epsilon_{e,n/s/p}$	Electrode/Separator porosity
$m_{n/p}$	Reaction rate $((A/m^2)(m^3/mol)^{1.5})$
$c_{e,typ}$	Typical electrolyte concentration (mol/m^3)
D_e	Electrolyte diffusivity (m^2/s)
κ	Electrolyte conductivity (S/m)
t^+	Cation transference number
b	Bruggeman coefficient
A	Electrode area (m^2)
U_{eq}	Equilibrium potential (V)
η_c	Overpotential due to electrolyte concentration gradients (V)
η_r	Charge transfer overpotential (V)
$\Delta\Phi_e$	Ohmic losses in the electrolyte (V)
$\Delta\Phi_s$	Ohmic losses in the solid (V)
$OCP_{n/p}$	Open Circuit Potential of Positive/Negative electrodes (V)
$\chi_{n/p}$	Normalized active material lithium concentration
F	Faraday's constant (C/mol)
R	Universal gas constant (J/K mol)
T	Temperature (K)
R_{ct}	Charge-transfer resistance (Ω)
Q	Cell capacity (Ah)

References

[1] G. Zubi, R. Dufo-López, M. Carvalho, G. Pasaoglu, The lithium-ion battery: State of the art and future perspectives, Renew. Sustain. Energy Rev. 89 (2018) 292–308, http://dx.doi.org/10.1016/j.rser.2018.03.002.

[2] J. Xie, Y.-C. Lu, A retrospective on lithium-ion batteries, Nature Commun. 11 (2020) 2499, http://dx.doi.org/10.1038/s41467-020-16259-9.

[3] D. Stampatori, P.P. Raimondi, M. Noussan, Li-ion batteries: A review of a key technology for transport decarbonization, Energies 13 (10) (2020) http://dx.doi.org/10.3390/en13102638.

[4] Y. Wang, J. Tian, Z. Sun, L. Wang, R. Xu, M. Li, Z. Chen, A comprehensive review of battery modeling and state estimation approaches for advanced battery management systems, Renew. Sustain. Energy Rev. 131 (2020) 110015, http://dx.doi.org/10.1016/j.rser.2020.110015.

[5] U.K. Das, P. Shrivastava, K.S. Tey, M.Y.I. Bin Idris, S. Mekhilef, E. Jamei, M. Seyedmahmoudian, A. Stojcevski, Advancement of lithium-ion battery cells voltage equalization techniques: A review, Renew. Sustain. Energy Rev. 134 (2020) 110227, http://dx.doi.org/10.1016/j.rser.2020.110227.

[6] K.M. Carthy, H. Gullapalli, K.M. Ryan, T. Kennedy, Review—Use of impedance spectroscopy for the estimation of Li-ion battery state of charge, state of health and internal temperature, J. Electrochem. Soc. 168 (8) (2021) 080517, http://dx.doi.org/10.1149/1945-7111/ac1a85.

[7] S. Wang, S. Jin, D. Bai, Y. Fan, H. Shi, C. Fernandez, A critical review of improved deep learning methods for the remaining useful life prediction of lithium-ion batteries, Energy Rep. 7 (2021) 5562–5574, http://dx.doi.org/10.1016/j.egyr.2021.08.182.

[8] T.F. Fuller, M. Doyle, J. Newman, Simulation and Optimization of the Dual Lithium Ion Insertion Cell, J. Electrochem. Soc. 141 (1) (1994) 1–10, http://dx.doi.org/10.1149/1.2054684.

[9] T.F. Fuller, J.E. Soc, T.F. Fuller, M. Doyle, J. Newman, Relaxation Phenomena in Lithium - Ion - Insertion Cells Relaxation Phenomena in Lithium-Ion-Insertion Cells, 1994.

[10] A. Jokar, B. Rajabloo, M. Désilets, M. Lacroix, Review of simplified Pseudo-two-Dimensional models of lithium-ion batteries, J. Power Sources 327 (2016) 44–55, http://dx.doi.org/10.1016/j.jpowsour.2016.07.036.

[11] D. Zhang, B.N. Popov, R.E. White, Modeling Lithium Intercalation of a Single Spinel Particle under Potentiodynamic Control, J. Electrochem. Soc. 147 (3) (2000) 831, http://dx.doi.org/10.1149/1.1393279.

[12] E. Prada, D.D. Domenico, Y. Creff, J. Bernard, V. Sauvant-Moynot, F. Huet, Simplified electrochemical and thermal model of $LiFePO_4$-graphite li-ion batteries for fast charge applications, J. Electrochem. Soc. 159 (9) (2012) A1508–A1519, http://dx.doi.org/10.1149/2.064209jes.

[13] G. Ning, B.N. Popov, Cycle life modeling of lithium-ion batteries, J. Electrochem. Soc. 151 (10) (2004) A1584, http://dx.doi.org/10.1149/1.1787631.

[14] S.G. Marquis, V. Sulzer, R. Timms, C.P. Please, S.J. Chapman, An Asymptotic Derivation of a Single Particle Model with Electrolyte, J. Electrochem. Soc. 166 (15) (2019) A3693–A3706, http://dx.doi.org/10.1149/2.0341915jes.

[15] S.J. Moura, F.B. Argomedo, R. Klein, A. Mirtabatabaei, M. Krstic, Battery state estimation for a single particle model with electrolyte dynamics, IEEE Trans. Control Syst. Technol. 25 (2) (2017) 453–468, http://dx.doi.org/10.1109/TCST.2016.2571663.

[16] S. Khaleghi Rahimian, S. Rayman, R.E. White, Extension of physics-based single particle model for higher charge–discharge rates, J. Power Sources 224 (2013) 180–194, http://dx.doi.org/10.1016/j.jpowsour.2012.09.084.

[17] X. Han, M. Ouyang, L. Lu, J. Li, Simplification of physics-based electrochemical model for lithium ion battery on electric vehicle. Part I: Diffusion simplification and single particle model, J. Power Sources 278 (2015) 802–813, http://dx.doi.org/10.1016/j.jpowsour.2014.12.101.

[18] J. Li, N. Lotfi, R.G. Landers, J. Park, A single particle model for lithium-ion batteries with electrolyte and stress-enhanced diffusion physics, J. Electrochem. Soc. 164 (4) (2017) A874–A883, http://dx.doi.org/10.1149/2.1541704jes.

[19] A. Romero-Becerril, L. Alvarez-Icaza, Comparison of discretization methods applied to the single-particle model of lithium-ion batteries, J. Power Sources 196 (23) (2011) 10267–10279, http://dx.doi.org/10.1016/j.jpowsour.2011.06.091.

[20] G. Plett, Battery Management Systems, Volume I: Battery Modeling, Artech House Power Engineering and Power Electronics, 2015.

[21] MathWorks, Simulink documentation: simulation and model-based design, 2020.

[22] J. Sabatier, M. Merveillaut, J.M. Francisco, F. Guillemard, D. Porcelatto, Lithium-ion batteries modeling involving fractional differentiation, J. Power Sources 262 (2014) 36–43, http://dx.doi.org/10.1016/j.jpowsour.2014.02.071.

[23] J. Sabatier, J.M. Francisco, F. Guillemard, L. Lavigne, M. Moze, M. Merveillaut, Lithium-ion batteries modeling: A simple fractional differentiation based model and its associated parameters estimation method, Signal Process. 107 (2015) 290–301, http://dx.doi.org/10.1016/j.sigpro.2014.06.008, Special Issue on ad hoc microphone arrays and wireless acoustic sensor networks Special Issue on Fractional Signal Processing and Applications.

[24] J. Sabatier, Power law type long memory behaviors modeled with distributed time delay systems, Fract. Fract. 4 (1) (2020) http://dx.doi.org/10.3390/fractalfract4010001.

[25] E. Miguel, G.L. Plett, M.S. Trimboli, L. Oca, U. Iraola, E. Bekaert, Review of computational parameter estimation methods for electrochemical models, J. Energy Storage 44 (2021) 103388, http://dx.doi.org/10.1016/j.est.2021.103388.

[26] D.U.S. Alexander Farmann, Comparative study of reduced order equivalent circuit models for on-board state-of-available-power prediction of lithium-ion batteries in electric vehicles, Appl. Energy 225 (2018) 1102–1122, http://dx.doi.org/10.1016/j.apenergy.2018.05.066.

[27] H. Ren, Y. Zhao, S. Chen, L. Yang, A comparative study of lumped equivalent circuit models of a lithium battery for state of charge prediction, Int. J. Energy Res. 43 (2019) 7306–7315, http://dx.doi.org/10.1002/er.4759.

[28] V. Talele, M.S. Patil, S. Panchal, R. Fraser, M. Fowler, S.R. Gunti, Novel metallic separator coupled composite phase change material passive thermal design for large format prismatic battery pack, J. Energy Storage 58 (2023) 106336, http://dx.doi.org/10.1016/j.est.2022.106336.

[29] W. Li, Y. Xie, X. Hu, M.-K. Tran, M. Fowler, S. Panchal, J. Zheng, K. Liu, An internal heating strategy for lithium-ion batteries without lithium plating based on self-adaptive alternating current pulse, IEEE Trans. Veh. Technol. (2022) 1–14, http://dx.doi.org/10.1109/TVT.2022.3229187.

[30] G. Plett, Battery Management Systems, Volume II: Equivalent-Circuit Methods, Artech House Power Engineering and Power Electronics, 2015.

[31] P. Shrivastava, T.K. Soon, M.Y.I.B. Idris, S. Mekhilef, Overview of model-based online state-of-charge estimation using Kalman filter family for lithium-ion batteries, Renew. Sustain. Energy Rev. 113 (2019) 109233, http://dx.doi.org/10.1016/j.rser.2019.06.040.

[32] X. Hu, F. Feng, K. Liu, L. Zhang, J. Xie, B. Liu, State estimation for advanced battery management: Key challenges and future trends, Renew. Sustain. Energy Rev. 114 (2019) 109334, http://dx.doi.org/10.1016/j.rser.2019.109334.

[33] J. Gomez, R. Nelson, E.E. Kalu, M.H. Weatherspoon, J.P. Zheng, Equivalent circuit model parameters of a high-power Li-ion battery: Thermal and state of charge effects, J. Power Sources 196 (10) (2011) 4826–4831, http://dx.doi.org/10.1016/j.jpowsour.2010.12.107.

[34] M. Bruch, L. Millet, J. Kowal, M. Vetter, Novel method for the parameterization of a reliable equivalent circuit model for the precise simulation of a battery cell's electric behavior, J. Power Sources 490 (2021) 229513, http://dx.doi.org/10.1016/j.jpowsour.2021.229513.

[35] P. Poopanya, K. Sivalertporn, T. Phophongviwat, A Comparative Study on the Parameter Identification of an Equivalent Circuit Model for an Li-ion Battery Based on Different Discharge Tests, World Electr. Veh. J. 13 (3) (2022) 1–13, http://dx.doi.org/10.3390/wevj13030050.

[36] M. Chen, G.A. Rincón-Mora, Accurate electrical battery model capable of predicting runtime and I-V performance, IEEE Trans. Energy Convers. 21 (2) (2006) 504–511, http://dx.doi.org/10.1109/TEC.2006.874229.

[37] C.R. Birkl, E. McTurk, M.R. Roberts, P.G. Bruce, D.A. Howey, A parametric open circuit voltage model for lithium ion batteries, J. Electrochem. Soc. 162 (12) (2015) A2271–A2280, http://dx.doi.org/10.1149/2.0331512jes.

[38] J.A. Lopez-Villanueva, S. Rodriguez-Bolivar, L. Parrilla, C. Finana, Simple Single Particle Model for Interpreting Fast Charge Results in Intercalation Batteries, Institute of Electrical and Electronics Engineers Inc., 2020, http://dx.doi.org/10.1109/DCIS51330.2020.9268676.

[39] C. Li, N. Cui, Z. Cui, C. Wang, C. Zhang, Novel equivalent circuit model for high-energy lithium-ion batteries considering the effect of nonlinear solid-phase diffusion, J. Power Sources 523 (December 2021) (2022) 230993, http://dx.doi.org/10.1016/j.jpowsour.2022.230993.

[40] X. Zhang, J. Lu, S. Yuan, J. Yang, X. Zhou, A novel method for identification of lithium-ion battery equivalent circuit model parameters considering electrochemical properties, J. Power Sources 345 (2017) 21–29, http://dx.doi.org/10.1016/j.jpowsour.2017.01.126.

[41] Y. Gao, C. Zhu, X. Zhang, B. Guo, Implementation and evaluation of a practical electrochemical- thermal model of lithium-ion batteries for EV battery management system, Energy 221 (2021) 119688, http://dx.doi.org/10.1016/j.energy.2020.119688.

[42] H. Pang, J. Jin, L. Wu, F. Zhang, K. Liu, A Comprehensive Physics-Based Equivalent-Circuit Model and State of Charge Estimation for Lithium-Ion Batteries, J. Electrochem. Soc. 168 (9) (2021) 090552, http://dx.doi.org/10.1149/1945-7111/ac2701.

[43] K. Khodadadi Sadabadi, P. Ramesh, Y. Guezennec, G. Rizzoni, Development of an electrochemical model for a lithium titanate oxide||nickel manganese cobalt battery module, J. Energy Storage 50 (2022) 104046, http://dx.doi.org/10.1016/j.est.2022.104046.

[44] N. Meddings, M. Heinrich, F. Overney, J.S. Lee, V. Ruiz, E. Napolitano, S. Seitz, G. Hinds, R. Raccichini, M. Gaberšček, J. Park, Application of electrochemical impedance spectroscopy to commercial Li-ion cells: A review, J. Power Sources 480 (May) (2020) http://dx.doi.org/10.1016/j.jpowsour.2020.228742.

[45] T. Momma, M. Matsunaga, D. Mukoyama, T. Osaka, Ac impedance analysis of lithium ion battery under temperature control, J. Power Sources 216 (2012) 304–307, http://dx.doi.org/10.1016/j.jpowsour.2012.05.095.

[46] S. Alavi, C. Birkl, D. Howey, Time-domain fitting of battery electrochemical impedance models, J. Power Sources 288 (2015) 345–352, http://dx.doi.org/10.1016/j.jpowsour.2015.04.099.

[47] Q. Zhang, D. Wang, B. Yang, H. Dong, C. Zhu, Z. Hao, An electrochemical impedance model of lithium-ion battery for electric vehicle application, J. Energy Storage 50 (2022) 104182, http://dx.doi.org/10.1016/j.est.2022.104182.

[48] T.P. Heins, N. Schlüter, S.T. Ernst, U. Schröder, On the interpretation of impedance spectra of large-format Lithium-Ion batteries and its application in aging studies, Energy Technol. 8 (2) (2020) 1900279, http://dx.doi.org/10.1002/ente.201900279.

[49] T. Heil, A. Jossen, Continuous approximation of the ZARC element with passive components, Meas. Sci. Technol. 32 (10) (2021) 104011, http://dx.doi.org/10.1088/1361-6501/ac0466.

[50] A. Oustaloup, F. Levron, B. Mathieu, F. Nanot, Frequency-band complex noninteger differentiator: characterization and synthesis, IEEE Trans. Circuits Syst. I 47 (1) (2000) 25–39, http://dx.doi.org/10.1109/81.817385.

[51] G. Tsirimokou, A systematic procedure for deriving RC networks of fractional-order elements emulators using MATLAB, AEU - Int. J. Electron. Commun. 78 (2017) 7–14, http://dx.doi.org/10.1016/j.aeue.2017.05.003.

[52] B.O. Agudelo, W. Zamboni, E. Monmasson, A comparison of time-domain implementation methods for fractional-order battery impedance models, Energies 14 (2021) 1–23, http://dx.doi.org/10.3390/en14154415.

[53] J.A. López-Villanueva, P. Rodríguez-Iturriaga, L. Parrilla, S. Rodríguez-Bolívar, A compact model of the ZARC for circuit simulators in the frequency and time domains, AEU - Int. J. Electron. Commun. (2022) 154293., http://dx.doi.org/10.1016/j.aeue.2022.154293.

[54] X. Hu, H. Yuan, C. Zou, Z. Li, L. Zhang, Co-estimation of state of charge and state of health for Lithium-Ion batteries based on fractional-order calculus, IEEE Trans. Veh. Technol. 67 (2018) 10319–10329, http://dx.doi.org/10.1109/TVT.2018.2865664.

[55] K.S. Mawonou, A. Eddahech, D. Dumur, D. Beauvois, E. Godoy, Improved state of charge estimation for Li-ion batteries using fractional order extended Kalman filter, J. Power Sources 435 (2019) 226710, http://dx.doi.org/10.1016/j.jpowsour.2019.226710.

[56] P. Rodríguez-Iturriaga, J.A. del Valle, S. Rodríguez-Bolívar, D. Anseán, J.C. Viera, J.A. López-Villanueva, A novel dual fractional-order extended Kalman filter for the improved estimation of battery state of charge, J. Energy Storage 56 (2022) 105810, http://dx.doi.org/10.1016/j.est.2022.105810.

[57] V. Sulzer, S.G. Marquis, R. Timms, M. Robinson, S.J. Chapman, Python Battery Mathematical Modelling (PyBaMM), J. Open Res. Softw. 9 (1) (2021) 14, http://dx.doi.org/10.5334/jors.309.

[58] M. Dubarry, G. Baure, Perspective on commercial Li-ion battery testing, best practices for simple and effective protocols, Electronics 9 (1) (2020) http://dx.doi.org/10.3390/electronics9010152.

[59] USABC electric vehicle Battery Test Procedures Manual. Revision 2, Tech. Rep., Office of Scientific and Technical Information (OSTI), 1996, http://dx.doi.org/10.2172/214312.

[60] C.-H. Chen, F.B. Planella, K. O'Regan, D. Gastol, W.D. Widanage, E. Kendrick, Development of experimental techniques for parameterization of multi-scale Lithium-ion battery models, J. Electrochem. Soc. 167 (8) (2020) 080534, http://dx.doi.org/10.1149/1945-7111/ab9050.

[61] X.-S. Yang, Chapter 7 - particle swarm optimization, in: X.-S. Yang (Ed.), Nature-Inspired Optimization Algorithms, Elsevier, Oxford, 2014, pp. 99–110, http://dx.doi.org/10.1016/B978-0-12-416743-8.00007-5.